

Magnetocapacitance Effect And Magnetoelectric Coupling In  
Type-II Multiferroics  $R\text{FeWO}_6$  ( $R = \text{Ho, Dy, and Tb}$ )

by  
Moein Adnani

A dissertation submitted to the Department of Physics,  
College of Natural Sciences and Mathematics  
in partial fulfillment of the requirements for the degree of

Doctor of Philosophy  
in Physics

Chair of Committee: Ching-Wu Chu

Committee Member: Zhifeng Ren

Committee Member: Allan Jacobson

Committee Member: Pavan Hosur

Committee Member: Wei-Kan Chu

University of Houston  
May 2021

Copyright 2021, Moein Adnani

## DEDICATION/EPIGRAPH

*Dedicated to my parents and my wife.*

فَأَصْبِرْ صَبْرًا جَمِيلًا  
إِنَّهُمْ يَرَوْنَهُ بَعِيدًا  
وَنَرَاهُ قَرِيبًا

Moein Adnani

May 12, 2021

## ACKNOWLEDGMENTS

I take this opportunity to express my gratitude and appreciation to the people that without their help and guidance I would not be able to finish this work.

First, I would like to thank my supervisor professor Paul C. W. Chu for providing me with the opportunity to work in his lab and take advantage of the excellent resources it offered. I am grateful for his support, criticisms, and guidance throughout my study and for the financial support that allowed me to attend a couple of conferences to meet and become familiar with research conducted by world-class scientists.

I would like to thank all of my committee members, Prof. Zhifeng Ren, Prof. Allan Jacobson, Dr. Pavan Hosur, and Prof. Wei-Kan Chu for the support and for attending and raising insightful questions during my annual progress reports, which allowed me to look at the challenges and problems from a different perspective. In particular, Prof. Jacobson for his help in getting me started with the Rietveld refinement analysis.

In addition, I would like to thank all of my friends, colleagues, and group members (current and alumni) at Prof. Chu's lab for their help, support, and companionship. My thanks and appreciations go to Dr. Liangzi Deng for his help and teaching me how to work with various instruments, especially MPMS3, and making efficient measurements; Dr. Zheng Wu for his assistance with various technical lab issues, especially during sample preparation and working with furnaces; Dr. Narayan Poudel, Dr. Melissa Gooch, and Dr. Hung-Cheng Wu for teaching me on making dielectric, polarization, and heat capacity measurements; Dr. Hanming Yuan, Dr. Rabin Dahal, and Dr. Shuyuan Huyuan for their help and discussions; and Troy Christensen for his assistance and help with the administrative affairs and reading and reviewing my manuscript and greatly improving its language.

I am grateful to my friends and colleagues Dr. Sayed Ali Akbar Ghorashi, Dr. Samira Daneshmandi, Dr. Taha Salavati-fard, and Dr. Hasan Salehi Najafabadi for all their help, support, encouragement, valuable discussions, and numerous coffee and lunchtimes together. It certainly helped me to endure and overcome the difficulties and obstacles on my way. Taha also collaborated on my research and patiently spent the time and effort to make the DFT calculations needed for my work and helped with writing the manuscript.

In addition, I would also like to thank my collaborators Dr. Stefano Agrestini, Dr. Eric Pellegrin, and Dr. Javier Herrero-Martin for their valuable efforts in making the XAS/XMCD measurements and analysis for the project, and Dr. Lars Grabow for his contribution to DFT calculation analysis and carefully reading the manuscript. I am especially thankful to Stefano for his effort and help in preparing the manuscript and responding to the questions by the referees.

Finally, I would like to thank my family; my parents, my sister, my father and mother in laws, and my wife. I will not be able to reach here and achieve what I have in life without the unconditional love, support, and sacrifice of my family. My parents selflessly put my education and success ahead of their comfort in life and I will be indebted to them for always. Nothing can replace sisterly love and I am thankful to have such a wonderful sister and for being near our parents while I am away. I am thankful for having a wonderful mother- and father-in-law and for all their help and support during these years. And my dear wife, I am always grateful for all her sacrifice, endurance, encouragement, and love for the past few years. Her presence and emotional support certainly gave me the strength to overcome the hardships through this journey.

## ABSTRACT

In this work, we have studied the multiferroic behavior and magnetoelectric (ME) coupling in a group of oxides,  $\text{RFeWO}_6$  ( $\text{R} = \text{Ho, Dy, and Tb}$ ). These compounds have a non-centrosymmetric polar structure (space group  $Pna2_1$ ) at room temperature and exhibit an onset of an improper ferroelectric transition with an antiferromagnetic ordering at the Néel temperature ( $T_N$ ). The magnetic properties of the polycrystalline samples were studied by DC and AC magnetization and heat capacity measurements. The metamagnetic behavior at low temperatures was found to be directly related to the dielectric properties and polarization of the compounds. We observed that the field-dependent measurements of capacitance show a magnetocapacitance (MC) effect with double-hysteresis loop behavior, which is in direct correspondence with the magnetization. Our X-ray diffraction results on  $\text{HoFeWO}_6$  show the  $Pna2_1$  structure down to 8 K and suggest the absence of a structural phase transition across  $T_N$ . The structural relaxation calculation of  $\text{HoFeWO}_6$  also shows that the  $Pna2_1$  is the stable structure. The total density of states of this compound also demonstrates an insulating state with a wide band gap of  $\sim 3.7$  eV. Soft X-ray absorption spectroscopy and soft X-ray magnetic circular dichroism (XMCD) measurements at the Fe  $L_{2,3}$  and R ( $= \text{Ho, Dy, and Tb}$ )  $M_{4,5}$  edges revealed the oxidation state of Fe and R ( $= \text{Ho, Dy, and Tb}$ ) cations to be 3+. Fe  $L_{2,3}$  XMCD further shows that  $\text{Fe}^{3+}$  cations are antiferromagnetically ordered in a non-collinear fashion with spins arranged 90 degrees with respect to each other. Our findings show that  $\text{HoFeWO}_6$ , in addition to  $\text{DyFeWO}_6$  and  $\text{TbFeWO}_6$ , is also a type-II multiferroic and they all exhibit an MC effect. The observed MC effect and the change in polarization by the magnetic field, in addition to their direct correspondence with magnetization, further support the strong ME coupling in this compound.

# TABLE OF CONTENTS

<b>DEDICATION</b>	<b>iii</b>
<b>ACKNOWLEDGMENTS</b>	<b>iv</b>
<b>ABSTRACT</b>	<b>v</b>
<b>LIST OF FIGURES</b>	<b>ix</b>
<b>LIST OF TABLES</b>	<b>x</b>
<b>1 INTRODUCTION</b>	<b>1</b>
<b>2 BACKGROUND</b>	<b>4</b>
2.1 Paramagnetism: Curie's law . . . . .	4
2.2 Magnetic Ordering in Solids: Ferromagnetism and Antiferromagnetism . . . . .	12
2.3 Dielectric Materials and Polarization . . . . .	15
2.4 Crystallographic Point Groups . . . . .	21
2.5 Piezoelectricity, Pyroelectricity, and Ferroelectricity . . . . .	21
2.6 Landau Theory of Phase Transition; Proper and Improper Ferroelectrics . . . . .	23
2.7 Multiferroics . . . . .	28
2.8 Magnetoelectric Coupling and Mechanisms for Induced Polarization . . . . .	29
<b>3 METHODS AND EXPERIMENTS</b>	<b>34</b>
3.1 Sample Preparation . . . . .	34
3.2 X-ray Diffraction and Rietveld Refinement . . . . .	35
3.3 X-ray Absorption Spectroscopy and X-ray Magnetic Circular Dichroism Spectroscopy	36
3.4 Density Functional Theory (DFT) Calculations . . . . .	36
3.5 Magnetic Property . . . . .	37
3.6 Physical Property Measurement System . . . . .	37
3.7 Dielectric Constant . . . . .	38
3.8 Pyroelectric Current and Polarization Measurement . . . . .	39
3.9 Specific Heat . . . . .	40
<b>4 RESULTS AND DISCUSSION</b>	<b>42</b>
4.1 Crystal Structure of $RFeWO_6$ ( $R = Ho, Dy, \text{ and } Tb$ ) . . . . .	42
4.2 X-ray absorption spectroscopy (XAS) and X-ray magnetic circular dichroism (XMCD) Results on $RFeWO_6$ ( $R = Ho, Dy, \text{ and } Tb$ ) . . . . .	47
4.3 Density Functional Theory (DFT) Calculations on $HoFeWO_6$ . . . . .	52
4.4 Magnetic Properties of $HoFeWO_6$ . . . . .	52
4.5 Magnetic Properties of $DyFeWO_6$ and $TbFeWO_6$ . . . . .	61
4.6 Ferroelectricity, Magnetocapacitance Effect and Magnetoelectric Coupling in $HoFeWO_6$	61
4.7 Magnetocapacitance Effect and Magnetoelectric Coupling in $DyFeWO_6$ and $TbFeWO_6$	69
<b>5 SUMMARY AND CONCLUSION</b>	<b>73</b>



## LIST OF FIGURES

1	Plot of the Brillouin function $B_J(x)$ for various values of the $J$ . . . . .	9
2	A schematic of different types of magnetic ordering and possible arrangement of spins. . . . .	13
3	A schematic of temperature dependent susceptibility and its inverse in different forms of magnetic ordering. . . . .	15
4	A schematic of different processes that contribute to the polarization of a dielectric. . . . .	17
5	A sketch of a cubic and centrosymmetric and a hexagonal non-centrosymmetric structure. . . . .	22
6	Venn diagram of different types of dielectric materials and the respective number of crystal classes. . . . .	23
7	Free energy as a function of order parameter and the order parameter as a function of temperature for the first- and second-order phase transition. . . . .	27
8	Local polarization generated by the anti-symmetric exchange interaction between canted adjacent spins. . . . .	32
9	Polarization generated by exchange interaction between two magnetic ions. . . . .	33
10	Thermal connection between sample and sample platform in the PPMS Heat Capacity Option. . . . .	41
11	Rietveld refinement of the room-temperature synchrotron XRD data for $\text{HoFeWO}_6$ . . . . .	43
12	Room-temperature synchrotron XRD pattern for $\text{HoFeWO}_6$ and the Rietveld refinement in logarithmic scale. . . . .	44
13	Room-temperature laboratory XRD pattern for $\text{HoFeWO}_6$ , $\text{DyFeWO}_6$ , and $\text{TbFeWO}_6$ . . . . .	44
14	Views of the crystal structure of $\text{HoFeWO}_6$ in different orientations. . . . .	45
15	Arrangement of $\text{Ho}^{3+}$ ions in the crystal, forming a quasi-one-dimensional chain along the $c$ direction. . . . .	45
16	Low temperature XRD pattern of $\text{HoFeWO}_6$ from 30–8 K. . . . .	47
17	Fe $L_{2,3}$ XAS spectrum of $\text{Fe}_2\text{O}_3$ as a reference, XAS and XMCD spectra of $\text{RFeWO}_6$ ( $\text{R} = \text{Ho, Dy, and Tb}$ ) measured at 2 K under a magnetic field of 6 T. . . . .	49
18	The measured R $M_{4,5}$ XAS and XMCD spectra of $\text{RFeWO}_6$ and the calculated XAS and XMCD of $\text{R}^{3+}$ for $\text{R} = \text{Ho, Dy, and Tb}$ . . . . .	51
19	Total density of states for $\text{HoFeWO}_6$ . Dashed line: Fermi energy. . . . .	54
20	Schematics of elemental and ionic Ho, Fe, and W atoms. . . . .	55
21	Temperature-dependent magnetic susceptibility of $\text{HoFeWO}_6$ and its inverse. . . . .	56
22	Heat capacity and magnified view of magnetic susceptibility of $\text{HoFeWO}_6$ . . . . .	57
23	Effect of magnetic field on DC magnetic susceptibility of $\text{HoFeWO}_6$ . . . . .	57
24	Real part of AC magnetic susceptibility of $\text{HoFeWO}_6$ . . . . .	58
25	Real part of AC magnetic susceptibility of $\text{HoFeWO}_6$ as function of temperature measured under different frequencies of $f = 10, 100, \text{ and } 1000$ Hz. . . . .	59
26	Field-dependent DC magnetization at different temperatures and its derivative. . . . .	60
27	Real part of AC magnetic susceptibility as a function of magnetic field measured at different temperatures. . . . .	60
28	DC magnetic susceptibility of $\text{DyFeWO}_6$ . . . . .	62
29	DC magnetic susceptibility of $\text{TbFeWO}_6$ . . . . .	62
30	Field-dependent DC magnetization of $\text{DyFeWO}_6$ at different temperatures and its derivative. . . . .	63

31	Field-dependent DC magnetization of $\text{TbFeWO}_6$ at different temperatures and its derivative. . . . .	63
32	Temperature-dependent dielectric constant and loss tangent of $\text{HoFeWO}_6$ under different magnetic fields. . . . .	65
33	Examples of pyrocurrent as a function of temperature measured for $\text{HoFeWO}_6$ under zero magnetic field. . . . .	66
34	Electric polarization as a function of temperature for $\text{HoFeWO}_6$ under different magnetic fields. . . . .	67
35	Field-dependent dielectric constant of $\text{HoFeWO}_6$ and its derivative at different temperatures. . . . .	68
36	Electric polarization as a function of field at different temperatures. . . . .	69
37	Capacitance of $\text{DyFeWO}_6$ and the loss tangent as a function of temperature. . . . .	70
38	Capacitance of $\text{TbFeWO}_6$ and the loss tangent as a function of temperature measured at different magnetic fields. . . . .	71
39	Field-dependent dielectric constant of $\text{DyFeWO}_6$ and its derivative at different temperatures. . . . .	72
40	Field-dependent dielectric constant of $\text{TbFeWO}_6$ and its derivative at different temperatures. . . . .	72

## LIST OF TABLES

1	Calculated and measured effective Bohr magneton for $\text{Tb}^{3+}$ , $\text{Dy}^{3+}$ , and $\text{Ho}^{3+}$ . . . . .	11
2	Calculated and measured effective Bohr magneton for $\text{Fe}^{3+}$ and $\text{Fe}^{2+}$ . . . . .	11
3	List of all the non-centrosymmetric crystal classes. . . . .	24
4	Structural and lattice parameters of $\text{HoFeWO}_6$ obtained from the Rietveld refinement of XRD data at $T = 300$ K. . . . .	46
5	Lattice parameters obtained from XRD at $T = 300$ K and $T = 8$ K and from DFT calculations. . . . .	47
6	Spin ( $m_s$ ) and orbital ( $m_l$ ) moments measured by XMCD. . . . .	50
7	Spin magnetic moments on the atoms in units of electron spin obtained by DFT calculations. . . . .	53

Copyright 2021, Moein Adnani

# 1 Introduction

Materials containing two or more ferroic orders have been the center of attention in the scientific community since they have great potential for devices with multiple controlling parameters as well as exhibiting novel physical phenomena and properties. This class of materials, formerly known as ferroelectromagnets and now as multiferroics, have long been known and extensively studied [1]. Interest in multiferroics was renewed in particular following the experimental observation of spin-induced polarization in rare-earth manganites and the theoretical explanation of its origin [2–9].

An interesting physical property exhibited by these compounds is magnetoelectric (ME) coupling or the mutual coupling between magnetic ordering and polarization [10, 11]. One way to indirectly investigate such coupling between spin and charge degree of freedom is through the magnetocapacitance (MC) effect.

Because of the common origin of ferroelectric polarization and magnetic ordering in type-II multiferroics, it is expected that the coupling between magnetic and ferroelectric ordering is relatively strong. Among the type-II multiferroics, orthorhombic rare-earth manganites, which have a non-polar crystal structure in the paramagnetic region, have been investigated intensively [7–9, 12, 13] and in fact, most known type-II multiferroics are centrosymmetric in the paramagnetic region.

Among materials having non-centrosymmetric crystal structure and exhibiting multiferroicity, well-known examples are  $\text{BiFeO}_3$  and hexagonal  $\text{YMnO}_3$ . They are categorized, however, as type-I multiferroics since their ferroelectricity and magnetic ordering have separate origins. While  $\text{Fe}^{3+}$  and  $\text{Mn}^{3+}$  are responsible for the magnetic state in the respective compounds, the ferroelectricity in  $\text{BiFeO}_3$  is caused by the lone pair electrons of the  $\text{Bi}^{3+}$  ions and that in  $\text{YMnO}_3$  is of improper geometric nature, in which topology determines its unconventional polarization domain properties. [14–18].

Several compounds with a non-centrosymmetric polar structure have also been reported to be magnetoelectric multiferroics, e.g.  $M_2Mo_3O_8$  ( $M=Fe, Mn$ ) [19–21],  $CaBaCo_4O_7$  [22–24],  $Ni_3TeO_6$  [25–27], and recently  $RFeWO_6$  ( $R=Dy, Eu, Tb, \text{ and } Y$ ) [28]. All of these compounds have a broken inversion symmetry in their paramagnetic region driven by the chemical ordering of their cations, and they show a change in polarization at the magnetic ordering temperature without any sign of structural phase transition, in which the polarization is coupled to the magnetic field.

It was proposed that these compounds should be classified as type-III, a new class of multiferroics, in order to distinguish them from type-II, in which the paramagnetic region is centrosymmetric and the magnetic ordering breaks the inversion symmetry, inducing a spontaneous polarization that is coupled to the magnetic field [29].

In aeschynite-type materials with the general formula of  $RMM'O_6$  ( $R$ =rare-earth;  $M, M'$ =transition metals), due to symmetry constraints, the crystal structure will adopt a polar space group,  $Pna2_1$  (no. 33), if  $M$  and  $M'$  are ordered [30]. It was previously reported that the oxides of  $RMWO_6$  ( $R$ =rare-earth element and  $M=V, Cr, \text{ and } Fe$ ) have an ordered arrangement of  $M^{3+}$  and  $W^{6+}$  and that they show an antiferromagnetic (AFM) ordering at low temperature [31]. In addition, it was recently shown by Ghara *et al.* [28] that the compounds of  $RFeWO_6$  ( $R=Dy, Eu, Tb, \text{ and } Y$ ) exhibit magnetoelectric multiferroicity. Their neutron diffraction study on  $DyFeWO_6$  revealed a commensurate non-collinear arrangement of  $Fe^{3+}$  and  $Dy^{3+}$  spins with the magnetic space group  $C_{2c}$ .

Here we studied the multiferroic behavior of polycrystalline samples of  $RFeWO_6$  ( $R = Ho, Dy, \text{ and } Tb$ ). The quality and crystal structure of the samples were confirmed using synchrotron X-ray diffraction (XRD). The X-ray absorption spectroscopy (XAS) measurements confirmed the 3+ valence state of the Fe and  $R$  cations. The X-ray magnetic circular dichroism (XMCD) spectrum

on the Fe  $L_{2,3}$  edge showed that the  $\text{Fe}^{3+}$  spins are arranged non-collinearly at angles of 90 degrees with respect to each other. Magnetic, dielectric, polarization, and heat capacity measurements showed that these compounds undergo an AFM ordering at the Néel temperature ( $T_N$ ) of 17.8, 18, and 15 K for  $R = \text{Ho}$ ,  $\text{Dy}$ , and  $\text{Tb}$ , respectively, which is accompanied by the onset of a ferroelectric transition at the same temperature. The magnetoelectric coupling was indirectly investigated further by measuring the capacitance as a function of the magnetic field. The direct correspondence of its capacitance and magnetization as functions of the magnetic field and the response of its polarization to the magnetic field indicates the presence of strong ME coupling in these compounds.

## 2 Background

In this chapter the key concepts and important phenomena pertaining to this research will be presented. This chapter starts by a review of magnetism in solids and different magnetic orderings. Then the basics of dielectric materials and ferroelectricity is discussed. At the end, the concept of multiferroicity, magnetoelectric coupling and different mechanisms of inducing polarization in multiferroics are explained.

### 2.1 Paramagnetism: Curie's law

Electrons have a characteristic angular momentum ( $\hbar\mathbf{s}$ ) which is associated with its spin degree of freedom. The spin magnetic moment is proportional to  $\mathbf{s}$  and is described as [32]:

$$\boldsymbol{\mu}_s = -g\mu_B\mathbf{s} \quad (1)$$

where  $\mu_B$  is called the Bohr magneton which has a magnitude of:

$$\begin{aligned} \mu_B &= \frac{e\hbar}{2mc} = 0.927 \times 10^{-20} \text{ erg/G} \\ &= 0.579 \times 10^{-8} \text{ eV/G}, \end{aligned} \quad (2)$$

where  $e$  is the magnitude of charge of electron,  $m$  its mass,  $c$  the velocity of light, and  $\hbar$  the Planck constant divided by  $2\pi$ . The  $g$ -value or the Landè  $g$ -factor is 2.

Electrons have an orbital magnetic moment, associated with their orbital motion, which can be

expressed as:

$$\boldsymbol{\mu}_o = -\frac{e}{2mc}(\mathbf{r} \times \mathbf{p}) = -\mu_B \mathbf{l} \quad (3)$$

where  $\mathbf{r}$  is the position vector of the electron,  $\mathbf{p}$  is its momentum, and  $\mathbf{l}$  is the angular momentum divided by  $\hbar$ . When a magnetic field  $\mathbf{H}$  is applied we can write

$$\begin{aligned} m\mathbf{v} &= \mathbf{p} + \frac{e}{c}\mathbf{A}(\mathbf{r}) \\ \Rightarrow \boldsymbol{\mu}_o(\mathbf{H}) &= -\mu_B \mathbf{l} - \frac{e^2}{2mc^2}(\mathbf{r} \times \mathbf{A}), \end{aligned} \quad (4)$$

where  $\mathbf{A}$  is the vector potential due to the external magnetic field, which is invariant under transformation to the vector potential  $\mathbf{A}'$  ( $\mathbf{A}' = \mathbf{A} + \nabla\chi$ ).

Similar to electrons, the atomic nuclei also have magnetic moment associated with the nuclear spin  $\mathbf{I}$ , which can be expressed as:

$$\boldsymbol{\mu} = g_N \mu_N \mathbf{I} \quad (5)$$

$\mu_N$  is called Nuclear Magneton and can be found using the Eq. 3 where the mass of electron  $m$  is replaced by the mass of proton  $M$ .  $\mu_N$  is corresponding to the  $g$ -value is of order of unity. In most cases the magnetic moments of atomic nuclei can be ignored in comparison with the magnetic moments of electrons as  $\mu_N = (1/1836)\mu_B$ .

For a quantum mechanical system at  $T = 0$  and with volume  $V$  inside a uniform magnetic field

$H$ , the magnetization density is defined as [33]:

$$M(H) = -\frac{1}{V} \frac{\partial E_0(H)}{\partial H} \quad (6)$$

where  $E_0(H)$  is the ground-state energy of the system inside field  $H$ . When the system is in thermal equilibrium at temperature  $T$ , the magnetization density has the form:

$$M = -\frac{1}{V} \frac{\partial F}{\partial H} \quad (7)$$

where  $F$  is the magnetic Helmholtz free energy and is defined as:

$$e^{-F/k_B T} = \sum_n e^{-E_n(H)/k_B T} \quad (8)$$

and the susceptibility is defined as

$$\chi = \frac{\partial M}{\partial H} \quad (9)$$

The Hamiltonian of the system in the presence of magnetic field is modified and by treating the change in the energy levels induced by the field as perturbation, the second-order perturbation theory gives:

$$E_n \rightarrow E_n + \Delta E_n; \quad \Delta E_n = \langle n | \Delta \mathbb{H} | n \rangle + \sum_{n' \neq n} \frac{|\langle n | \Delta \mathbb{H} | n' \rangle|^2}{E_n - E_{n'}} \quad (10)$$

and therefore we find:

$$\begin{aligned} \Delta E_n = \mu_B \mathbf{H} \cdot \langle n | \mathbf{L} + g_0 \mathbf{S} | n \rangle + \sum_{n' \neq n} \frac{|\langle n | \mu_B \mathbf{H} \cdot (\mathbf{L} + g_0 \mathbf{S}) | n' \rangle|^2}{E_n - E_{n'}} \\ + \frac{e^2}{8mc^2} H^2 \langle n | \sum_i (x_i^2 + y_i^2) | n \rangle \end{aligned} \quad (11)$$

The equation above can be used to determine the magnetic susceptibility of individual atoms, ions or molecules. It can also be used to determine the susceptibilities of solids that can be considered as a collection of slightly deformed individual ions [33].

(i) In case of a solid composed of ions with all electronic shells filled, the spin and orbital angular momentum in the ground state is zero;  $\mathbf{J}|0\rangle = \mathbf{L}|0\rangle = \mathbf{S}|0\rangle = 0$ . In this case only the third term in the Eq. 12 will contribute to the field-induced shift in the ground-state energy. As a result, the susceptibility of a solid composed of  $N$  ions in their ground state in thermal equilibrium is given by

$$\chi = -\frac{N}{V} \frac{\partial^2 \Delta E_0}{\partial H^2} = -\frac{e^2}{6mc^2} \frac{N}{V} \langle 0 | \sum_i r_i^2 | 0 \rangle \quad (12)$$

This term is known as the *Larmor diamagnetic susceptibility*. Diamagnetism means negative susceptibility and occurs in solid noble gases and alkali halides, in which the induced moment is opposite of the applied field. The molar susceptibility ( $\chi^{molar}$ ) can be found by multiplying the  $\chi$  by the volume of a mole,  $N_A/[N/V]$ , where  $N_A$  is the Avogadro number.

$$\begin{aligned} \chi^{molar} = -Z_i N_A \frac{e^2}{6mc^2} \langle r^2 \rangle = -Z_i \left( \frac{e^2}{\hbar c} \right)^2 \frac{N_A a_0^3}{6} \langle (r/a_0)^2 \rangle \\ \langle r^2 \rangle = \frac{1}{Z_i} \sum \langle 0 | r_i^2 | 0 \rangle \end{aligned} \quad (13)$$

where  $\langle r^2 \rangle$  is the mean square ionic radius,  $Z_i$  is the total number of electrons in the ion. By taking into account the values  $a_0 = 0.529 \text{ \AA}$ ,  $e^2/\hbar c = 1/137$ , we will have

$$\chi^{molar} = -0.79Z_i \times 10^{-6} \langle (r/a_0)^2 \rangle \text{ cm}^3/\text{mole} \quad (14)$$

(ii) When the solid contains ions with partially filled electronic shells, there are two cases that needs to be considered.

1. If the shell has  $J = 0$ , which is the case for shells with one electron short of being half filled, then the first term in Eq. 12 would be zero. Therefore, the susceptibility for a solid contains of  $N/V$  ions per volume is

$$\begin{aligned} \chi &= -\frac{N}{V} \frac{\partial^2 \Delta E_0}{\partial H^2} \\ &= -\frac{N}{V} \left[ \frac{e^2}{4mc^2} \langle 0 | \sum_i (x_i^2 + y_i^2) | 0 \rangle - 2\mu_B^2 \sum_n \frac{|\langle 0 | \mathbf{L}_z + g_0 \mathbf{S}_z | n \rangle|^2}{E_n - E_0} \right] \end{aligned} \quad (15)$$

The first term, as we saw before, is the Larmor diamagnetic susceptibility. The second term favors the alignment of the moment parallel to the field, which is called paramagnetic behavior. This paramagnetic correction to the Larmor diamagnetic susceptibility is known as *Van Vleck paramagnetism*.

2. If the shell does not have  $J = 0$ , then the first term in Eq. 12 does not vanish and its magnitude is so much larger than the other term that they can be ignored. In this situation the ground state is  $(2J + 1)$ -fold degenerate and if the splitting between the zero-field atomic ground-state is large compared with  $k_B T$ , then only the  $(2J + 1)$  states in the ground-state multiplet will contribute to the free energy.

If only the lowest  $(2J + 1)$  states are thermally excited, the magnetization for  $N$  ions in a volume

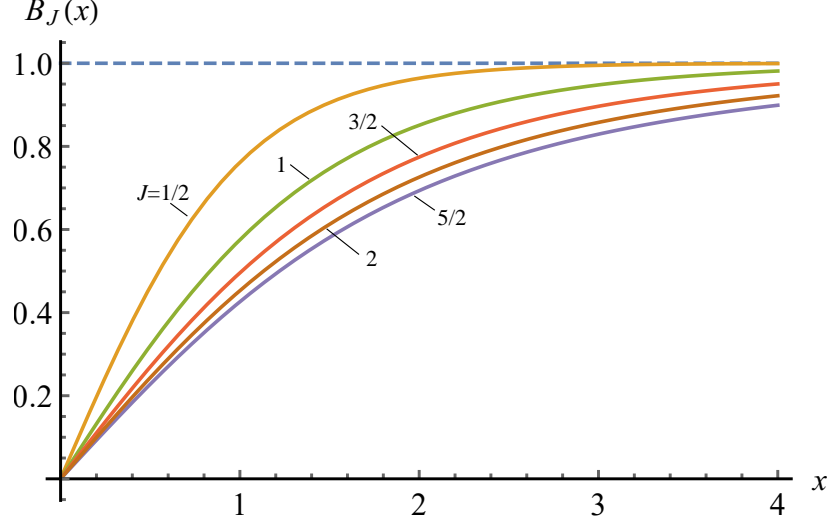


Figure 1: Plot of the Brillouin function  $B_J(x)$  for various values of the  $J$ .

$V$  is

$$M = -\frac{N}{V} \frac{\partial F}{\partial H} = \frac{N}{V} \gamma J B_J(\beta \gamma J H) \quad (16)$$

where

$$B_J(x) = \frac{2J+1}{2J} \coth \frac{2J+1}{2J} x - \frac{1}{2J} \coth \frac{1}{2J} x$$

$$\gamma = g(JLS)\mu_B$$

$B_J(x)$  in the equation above is the *Brillouin function*, and the  $g(JLS)$  is the Landé  $g$ -factor.

$$g(JLS) = \frac{3}{2} + \frac{1}{2} \left[ \frac{S(S+1) - L(L+1)}{J(J+1)} \right] \quad (17)$$

Figure 1 shows a plot of Brillouin function for different values of  $J$ . Under condition  $\gamma H \ll k_B T$ ,

we can use the small- $x$  expansion, which results in

$$\begin{aligned} \coth x &\approx \frac{1}{x} + \frac{1}{3}x + O(x^3), & B_J(x) &\approx \frac{J+1}{3J}x + O(x^3) \\ \implies \chi &= \frac{N}{V} \frac{(g\mu_B)^2}{3} \frac{J(J+1)}{k_B T}, & (k_B T &\gg g\mu_B H) \\ \chi^{molar} &= N_A \frac{(g\mu_B)^2}{3} \frac{J(J+1)}{k_B T} \end{aligned} \quad (18)$$

The relationship above, which shows the change of susceptibility with respect to inverse of temperature is known as *Curie's law*.

It is worth pointing out that the paramagnetic susceptibility at room-temperature is larger than the temperature-independent diamagnetic susceptibility by a factor of order 500, therefore, when an ion with partially filled shell with  $J \neq 0$  is present in a solid, the contribution of this shell to the total magnetic susceptibility of the material is much larger than the diamagnetic contribution from the other filled shells. Insulating crystals with rare-earth ions are one of the commons materials to obey the Curie's law. The Curie's law is frequently written in the following form:

$$\chi = \frac{1}{3} \frac{N}{V} \frac{\mu_B^2 p^2}{k_B T} \quad (19)$$

where  $p$  is the effective Bohr magneton number.

$$p = g(JLS)[J(J+1)]^{1/2} \quad (20)$$

Table 1 compares the value of the  $p$  for the rare-earth elements used in this study (Ho, Dy, and Tb) obtained from the coefficient of  $1/T$  in the measured susceptibility and the values determined from the Eq. 17 and 20 [33].

Table 1: Calculated and measured effective Bohr magneton for  $\text{Tb}^{3+}$ ,  $\text{Dy}^{3+}$ , and  $\text{Ho}^{3+}$ . The data are adopted from the reference [33].

Element	Basic Electron	Ground-state	Calculation	Measurement
	Configuration	Term		
Tb	$4f^8$	${}^7F_6$	9.72	9.5
Dy	$4f^9$	${}^6H_{15/2}$	10.63	10.6
Ho	$4f^{10}$	${}^5I_8$	10.60	10.4

The magnetism of rare-earth ions in an insulating solid can be well described by considering them as isolated ions. In case of transition metal ions the Curie's law is satisfied, however, the orbital angular momentum is *quenched* due to crystal field splitting. This means that the value of effective Bohr magneton  $p$  is determined by considering the  $L$  as zero and hence  $J$  is equal to  $S$ . Table 2 shows the calculated and measured values of  $p$  for the  $\text{Fe}^{3+}$  and  $\text{Fe}^{2+}$  [33].

Table 2: Calculated and measured effective Bohr magneton for  $\text{Fe}^{3+}$  and  $\text{Fe}^{2+}$ . The data are adopted from the reference [33].

Element	Basic Electron	Ground-state	Calculation		Measurement
	Configuration	Term	$(J = S)$	$(J =  L + S )$	
$\text{Fe}^{3+}$	$3d^5$	${}^6S_{5/2}$	5.92	5.92	5.9
$\text{Fe}^{2+}$	$3d^6$	${}^5D_4$	4.90	6.70	5.4

In majority of magnetic ionic crystals or rare-earth metals, the electrons in the partially filled shells are in a localized state but are influenced by the surrounding ions, known as crystal-field effect. This effect in the  $3d$  partially filled transition metals is much larger than in the  $4f$  shell of rare-earth metals as the  $3d$  electrons are located in the outermost shell of the ion and it directly interacts with the electrons in the surrounding ions while the  $4f$  shells of rare-earth ions lies deep inside the ion beneath filled  $5s$  and  $5p$  shells [32].

Unlike the electrons in the partially filled ionic shells, the conduction electrons of a metals are not spatially localized and the Curie's law does not apply to them. The magnetic susceptibility of conduction electrons can be found from the following relationship

$$\chi = \mu_B^2 g(\mathcal{E}_F) \quad (21)$$

where  $g(\mathcal{E}_F)$  is the density of levels at Fermi energy. This is known as the *Pauli paramagnetic susceptibility*. The Pauli susceptibility, in contrast to Curie's law, is independent of temperature.

In the case of free electron case, the Pauli susceptibility takes the following form

$$\chi_{\text{Pauli}} = \left(\frac{\alpha}{2\pi}\right)^2 (a_0 k_F) \quad (22)$$

$$\alpha = e^2/\hbar c = 1/137$$

$$\chi_{\text{Pauli}} = \left(\frac{2.59}{r_s/a_0}\right)^{-6}$$

## 2.2 Magnetic Ordering in Solids: Ferromagnetism and Antiferromagnetism

In the absence of magnetic interactions, individual magnetic moments would be thermally disordered and the vector moments would average to zero. In certain solids, individual magnetic ions show a non-vanishing average vector moment below a critical temperature  $T_c$ , which are called *magnetically ordered*.

The localized moments of ions in a magnetically ordered solid may or may not show a net magnetization density. If there exist a macroscopic bulk magnetization in the absence of external magnetic field (known as spontaneous magnetization), then the this ordered state is called *ferromagnetic*. If the individual local moments sum to zero without spontaneous magnetization, this

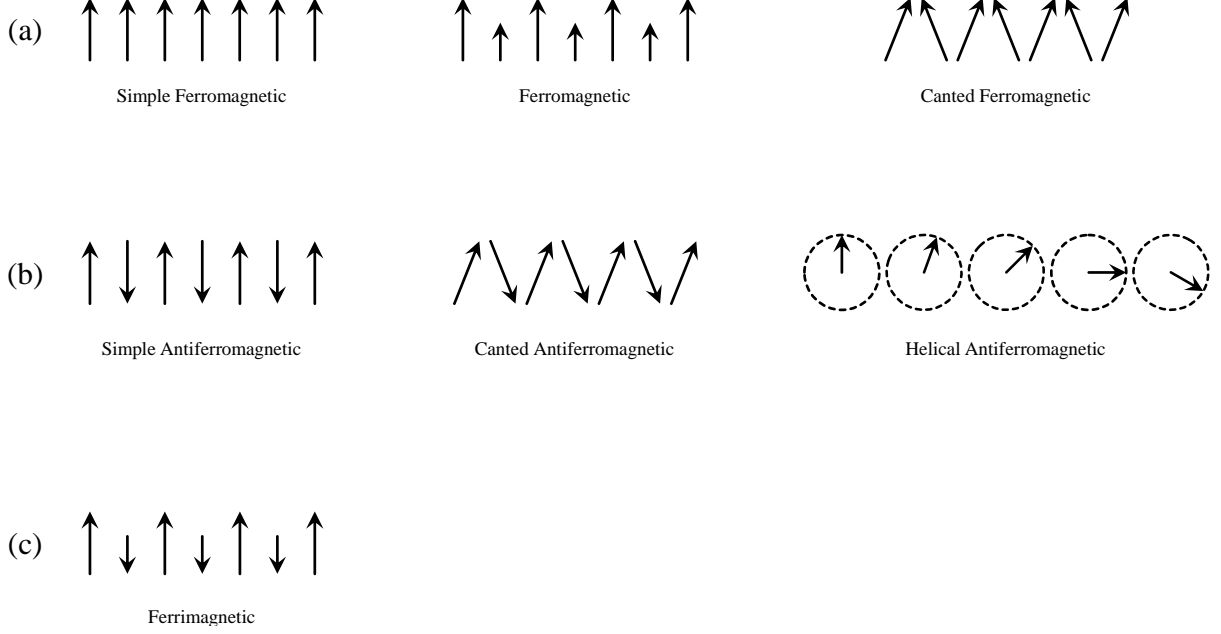


Figure 2: A schematic of different types of magnetic ordering and possible arrangement of spins in a (a) ferromagnetic, (b) antiferromagnetic, and (c) ferrimagnetic state.

ordered state is known as *antiferromagnetic*. When there are more than one magnetic ion in the solid and not *all* the local moments have a positive component along the direction of the spontaneous magnetization, this ordered state is called *ferrimagnetic*. Figure 2 shows a schematic of examples of different types of magnetic ordering.

The earliest attempt at quantitatively explain the ferromagnetic transition was through the mean (or molecular) field theory by P. Weiss, in which it assumes that the effect of interaction between the spins is to replace the field each spin feels by an effective field. Using this approximation the magnetization density can be written as

$$M = M_0 \left( \frac{H_{eff}}{T} \right) \quad (23)$$

where  $H_{eff} = H + \lambda M$  is the effective field and  $M_0$  is the magnetization density in the field  $H$  and

temperature  $T$  in the absence of magnetic interaction, which would be the same as in Eq. 16. When there is a spontaneous magnetization  $M(T)$  at temperature  $T$  (below the critical temperature  $T_c$ , known as Curie temperature) then at  $H = 0$  the Eq. above should give a nonzero answer

$$M(T) = M_0 \left( \frac{\lambda M}{T} \right) \quad (24)$$

The susceptibility in the mean field approximation is given by

$$\begin{aligned} \chi &= \frac{\partial M}{\partial H} = \frac{\partial M_0}{\partial H_{eff}} \frac{\partial H_{eff}}{\partial H} = \chi_0(1 + \lambda\chi) \\ \Rightarrow \chi &= \frac{\chi_0}{1 - \lambda\chi_0} \end{aligned} \quad (25)$$

where  $\chi_0$  is evaluated in the field  $H_{eff}$ . Above the critical temperature  $T_c$  and in the limit of zero applied field,  $\chi_0$  takes the form of Curie's law ( $\propto 1/T$ ) and the zero-field susceptibility becomes

$$\chi = \frac{\chi_0}{1 - (T_c/T)} \quad (26)$$

This equation is similar to the Curie's law for an ideal paramagnet, except that  $T$  is replaced by  $T - T_c$ . This modification is known as *Curie-Weiss* law.

In antiferromagnets, the spins will order in an antiparallel fashion below the critical temperature  $T_N$  called Néel temperature. The susceptibility in an antiferromagnet has the form of the Curie's law except that the temperature  $T$  is replaced by  $T + \theta_{CW}$ . This is similar to the case of the ferromagnetic ordering, however, the sign of the critical temperature is opposite.

The Curie-Weiss law, in spite of its inadequacy, offers a simple way to sort out the possible types of magnetic structure that may arise below the critical temperature. Figure 3 shows an illustration

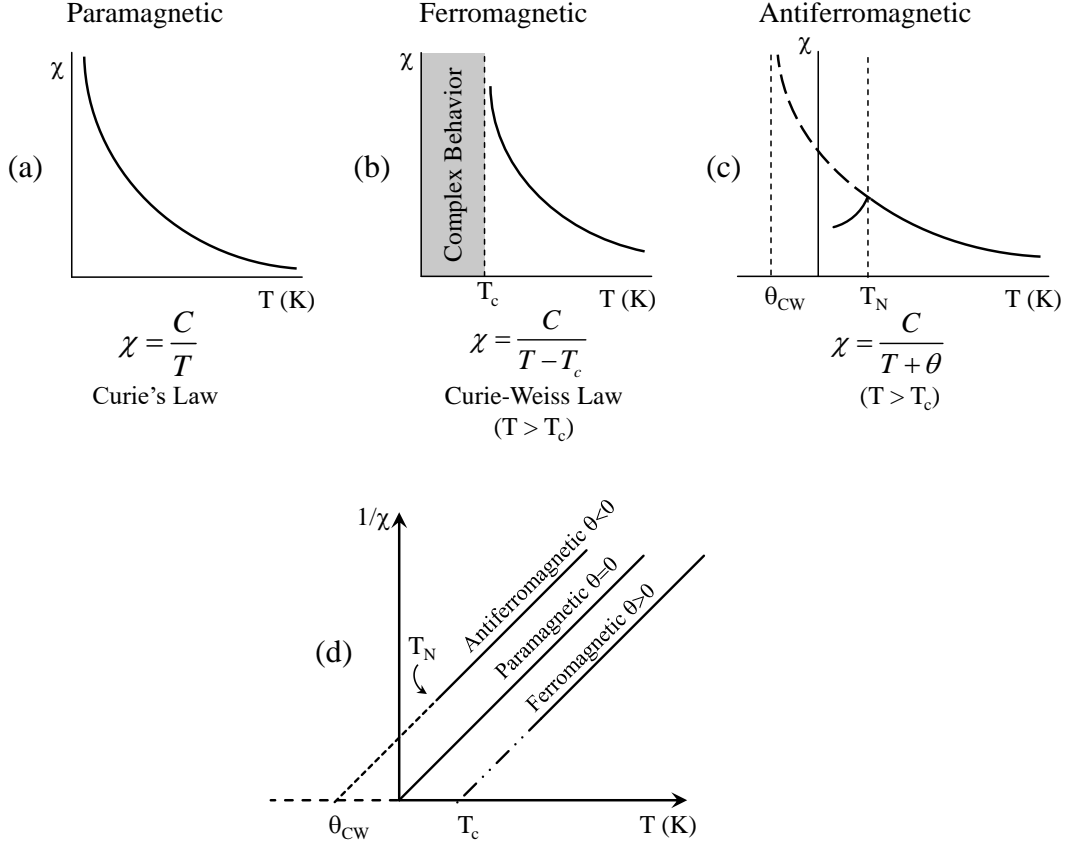


Figure 3: A schematic of temperature dependent susceptibility in a (a) paramagnet, (b) ferromagnet, and (c) antiferromagnet. (d) The inverse of susceptibility in different forms of magnetic ordering [34].

of the magnetic susceptibility in different types of ordering and its inverse with different signs of  $T_c$  or  $\theta_{CW}$  in the Curie-Weiss law.

### 2.3 Dielectric Materials and Polarization

A *dielectric* is an electrically insulating material, which can be polarized in the presence of an external electric field. The band gap in dielectrics is of order  $\sim 3$  eV or more, which prevents the electrons from thermal excitation from valence band to the conduction band. The formation of electric dipole moments and their orientation with the electric field determines the electric polarization of the dielectric. There are different factors that contributes to the polarization, which

are as follow [35]:

*Electronic* polarization ( $P_e$ ). When a neutral atom is placed inside an electric field, it shifts the electric charge of an atomic shell and the nucleus apart from each other, causing the center of charges to displace from the center of atom. This procedure induces a dipole moment. The electronic polarization is independent of temperature and directly proportional to the strength of the field.

*Ionic* polarization ( $P_i$ ). When ions of opposite charges are placed in an electric field, the positive ions move in the direction of the field and the negative ions move in opposite direction. This creates dipole moments and polarization which is also independent of temperature but depends on the binding energy of the ions in the lattice.

*Orientalional* polarization  $P_o$ . The permanent dipole moments in a dielectric, created by asymmetric distribution of charges between different atoms, will reorient themselves when placed in an electric field. This will contribute to the overall polarization. The orientational polarization depends on temperature and as temperature is increased the thermal energy tends to randomize the orientation of the dipole moments.

*Space (surface) charge* polarization  $P_s$ . In dielectrics there exist free charges that can move inside when the dielectric is placed in an electric field. These free charges can be trapped by the defects inside the dielectric and create a space charge. These space charges form a dipole moments, which contribute to the overall polarization. This polarization is also temperature dependent.

Figure 4 shows a drawing of summary of different process that contributes to the polarization of a dielectric.

When polarization within the material is uniform then the macroscopic field inside the body

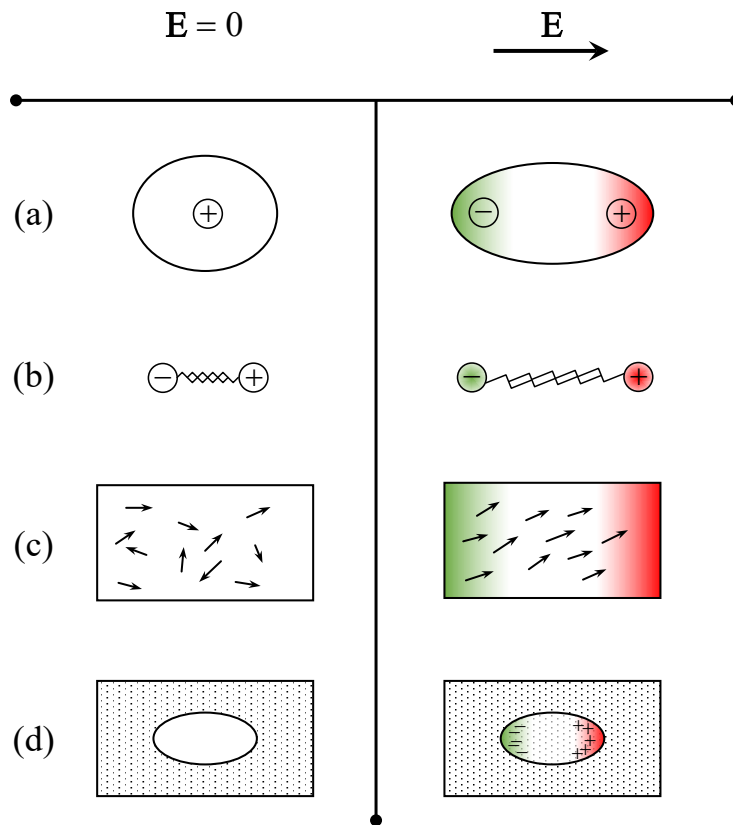


Figure 4: A schematic of different processes that contribute to the polarization of a dielectric: (a) electronic polarization, (b) ionic polarization, (c) orientational polarization, and (d) space charge polarization.

can be written as:

$$\begin{aligned}\mathbf{E} &= \mathbf{E}_0 + \mathbf{E}_1 \\ &= \mathbf{E}_0 - \frac{4\pi}{3}\mathbf{P}\end{aligned}\tag{27}$$

where  $\mathbf{E}_0$  is the applied field and the  $\mathbf{E}_1$  is the field caused by the uniform polarization in the material.  $\mathbf{E}_1$  is called the *depolarization field* and it opposes the applied field  $\mathbf{E}_0$ . The  $\mathbf{E}_1$  has a form  $\mathbf{E}_1 = -N\mathbf{P}$  where  $N$  is called the *depolarization factor* and depends on the shape of the object. For the case of a sphere  $N = 4\pi/3$ .

The *dielectric susceptibility* ( $\chi$ ) can be defined as

$$\mathbf{P} = \chi\mathbf{E}\tag{28}$$

so it would connect the macroscopic field inside the body to the polarization. The *dielectric constant* ( $\epsilon$ ) can also be defined as

$$\epsilon \equiv \frac{E + 4\pi P}{E} = 1 + 4\pi\chi\tag{29}$$

It is also worth mentioning that the results above are derived in CGS unit and in order to obtain the same results in the SI unit, we can use the conversion  $\chi_{SI} = 4\pi\chi_{CGS}$  and by definition  $\epsilon_{SI} = \epsilon_{CGS}$ .

Another quantity that is usually used in the literature and textbooks is the *permittivity* or *absolute permittivity* of the medium, which is denoted also by ( $\epsilon$ ) and can be mistaken with the dielectric constant. The dielectric constant defined previously is sometimes denoted by ( $\kappa$ ) and also sometimes is called *relative permittivity*, which is related to the *permittivity* of the medium by

dividing it by the permittivity of the free space.

$$\epsilon = \kappa = \epsilon_r = \frac{\epsilon}{\epsilon_0} \quad (30)$$

where  $\epsilon_0$  is the permittivity of the space.

While it is more convenient to work with macroscopic field, it is also important to deal with the microscopic field acting on individual ions. Local microscopic field at the position of each ions determines the force acting on each individual ion and the resultant displacement and distortion of ions. This so called *local* field is significantly different from the macroscopic field at the same location. In order to evaluate the local field at  $\mathbf{r}$  (denoted by a prime sign:  $\mathbf{E}'(\mathbf{r})$ ), we consider a cubic arrangement of ions in a crystal of spherical shape. Then,  $\mathbf{E}'(\mathbf{r})$  is consist of contribution from sources of field from points *near* or *far* region from  $\mathbf{r}$ . The near or far region is defined as a sphere of radius  $\mathbf{r}'$  about  $\mathbf{r}$ , where the radius is small on the macroscopic scale, but it is large compared with the characteristic atomic dimensions  $a$ . In this case the local electric field can be written as:

$$\mathbf{E}'(\mathbf{r}) = \mathbf{E}'_{\text{near}}(\mathbf{r}) + \mathbf{E}'_{\text{far}}(\mathbf{r}) = \mathbf{E}'_{\text{near}}(\mathbf{r}) + \mathbf{E}_{\text{far}}(\mathbf{r}) \quad (31)$$

where the local field of far region ( $\mathbf{E}'_{\text{far}}(\mathbf{r})$ ) is replaced by the macroscopic field of the far region ( $\mathbf{E}_{\text{far}}(\mathbf{r})$ ) as the contribution from the local field of far region has a negligible variation over a small distance (of order  $a$ ) and therefore we use an averaged value of macroscopic field from far region.

The full macroscopic field at  $\mathbf{r}$  can be divided into contribution from near and far region:

$$\mathbf{E}(\mathbf{r}) = \mathbf{E}_{\text{near}}(\mathbf{r}) + \mathbf{E}_{\text{far}}(\mathbf{r}) \quad (32)$$

therefore, the local field can be written as

$$\mathbf{E}'(\mathbf{r}) = \mathbf{E}(\mathbf{r}) + \mathbf{E}'_{\text{near}}(\mathbf{r}) - \mathbf{E}_{\text{near}}(\mathbf{r}) \quad (33)$$

the  $\mathbf{E}_{\text{near}}(\mathbf{r})$  which, in essence, is the macroscopic field from a uniformly polarized region of spherical shape is just  $\mathbf{E} = -4\pi\mathbf{P}/3$ . In the case when the near region is a specimen of spherical shape and a cubic environment for each point, the local field from this region will vanish and as a result the local field at point  $\mathbf{r}$  will become:

$$\mathbf{E}'(\mathbf{r}) = \mathbf{E}(\mathbf{r}) + \frac{4\pi}{3}\mathbf{P}(\mathbf{r}) \quad (34)$$

this result is also known as *Lorentz relation*. The Lorentz relation can be written in terms of dielectric constant ( $\epsilon$ ) as well:

$$\mathbf{D}(\mathbf{r}) = \epsilon\mathbf{E}(\mathbf{r})$$

where

$$\mathbf{D}(\mathbf{r}) = \mathbf{E}(\mathbf{r}) + 4\pi\mathbf{P}(\mathbf{r})$$

therefore

$$\mathbf{P}(\mathbf{r}) = \frac{\epsilon - 1}{4\pi}\mathbf{E}(\mathbf{r}) \quad (35)$$

$$\Rightarrow \mathbf{E}'(\mathbf{r}) = \frac{\epsilon + 2}{3}\mathbf{E}(\mathbf{r}) \quad (36)$$

This result can also be described in terms a quantity called *polarizability* ( $\alpha$ ) of a medium, in which polarizability of an ions at position  $\mathbf{d}$  is defined as the ration of induced dipole moment to the field

acting on it and the total polarizability is the sum of polarizabilities of all ions in the primitive cell.

$$\begin{aligned}\mathbf{P}(\mathbf{r}) &= \frac{\alpha}{v} \mathbf{E}'(\mathbf{r}) \\ \frac{\epsilon - 1}{\epsilon + 2} &= \frac{4\pi\alpha}{3v}\end{aligned}\tag{37}$$

The Eq. 37 is known as *Clausius-Mossotti* relation and links the macroscopic and microscopic theories.

## 2.4 Crystallographic Point Groups

A crystallographic *point group* is defined as a group of symmetry operations, which all of them map a lattice point onto itself [36]. There are 32 point groups in total. A single rotation and rotary-inversion (1, 2, 3, 4, and 6;  $\bar{1}$ ,  $\bar{2} = m$ ,  $\bar{3}$ ,  $\bar{4}$ ,  $\bar{6}$ ) can produce 10 point groups and the remaining 22 result from the combination of these 10 points groups [for example a two-fold axis perpendicular to another axis (*e.g.* 422), or mirror plane perpendicular to another axis (*e.g.* 2/*m*) or parallel to another axis (*e.g.* *mm2*)]. If crystal has a point of inversion then it is called *centrosymmetric* and if it lacks a point of inversion (a broken inversion symmetry) then it is called *non-centrosymmetric*. Figure 5 shows a sketch of a centrosymmetric and a non-centrosymmetric structure. There are 11 centrosymmetric and 21 non-centrosymmetric point groups.

## 2.5 Piezoelectricity, Pyroelectricity, and Ferroelectricity

*Piezoelectric* effect is the emergence of polarization in the material when it is subject to a mechanical stress and, conversely, the change of their shape and size when they are placed in electric field. This property is closely related to the symmetry of the crystal structure. Piezoelectric materials have a *non-centrosymmetric* crystal structure and from the 21 non-centrosymmetric point groups, 20 are

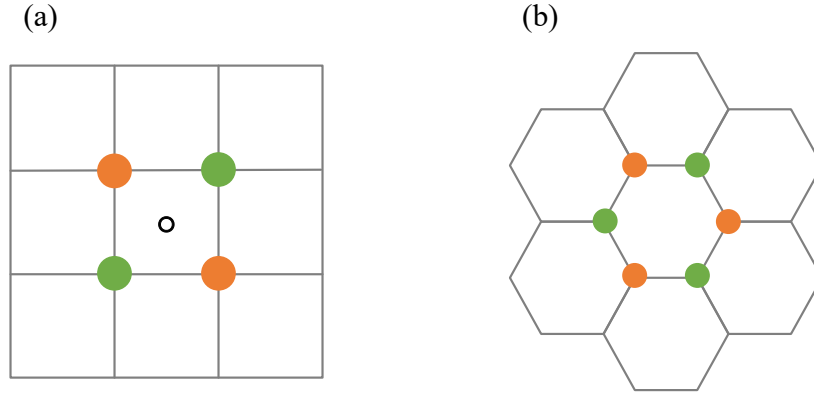


Figure 5: A sketch of (a) a cubic and centrosymmetric and (b) a hexagonal non-centrosymmetric structure. The small circle at the center of cubic structure is the center of inversion.

piezoelectric.

There are 10 point groups among piezoelectrics that have a *polar* crystal structure. A polar point group is one, for which, every symmetry operation leaves *more than one* common point unmoved [37]. In polar crystals the center of positive and negative charges do not coincide and as a result they exhibit a temperature-dependent spontaneous polarization. The polarization in these materials is usually masked by twinning or the surface bound charges. In this case, the polarization is revealed when the temperature in the whole material is changed uniformly, and a current will release from the material that can flow in an external circuit [38–40]. This effect is called *pyroelectricity* and materials exhibiting this effect are called pyroelectrics.

There is a special case of pyroelectric materials called *ferroelectrics*, in which, the direction of the polarization can be switch by application of a field of certain strength and in an oscillating electric field they will show a hysteresis. Ferroelectric materials have a certain transition temperature, called *curie temperature*  $T_c$ , below which the polarization appears. During the transition the crystal structure changes from a high symmetry state called paraelectric to the lower symmetry state of ferroelectric.

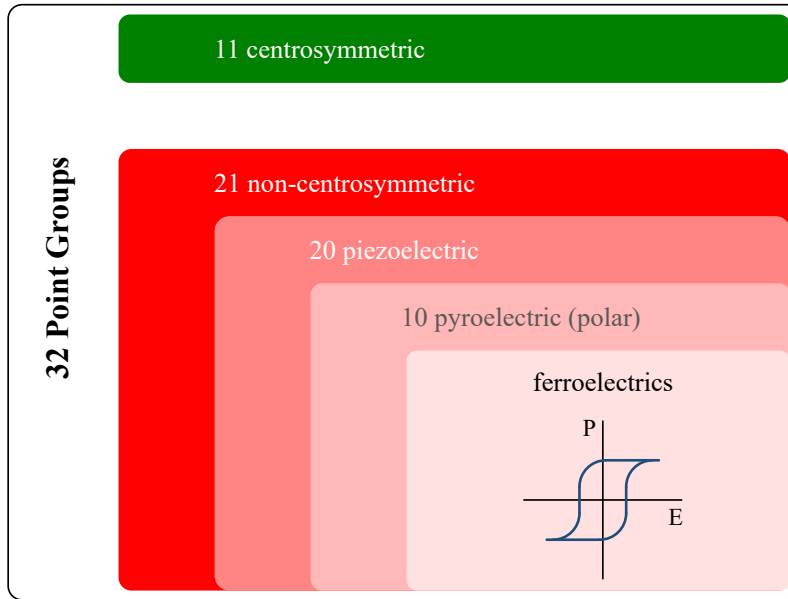


Figure 6: Venn diagram of different types of dielectric materials and the respective number of crystal classes.

Figure 6 shows a schematic Venn diagram depicting that ferroelectric materials are special subset of non-centrosymmetric materials. Table 3 shows the list of all the non-centrosymmetric crystal classes and the occurrence of piezoelectricity and pyroelectricity [37].

## 2.6 Landau Theory of Phase Transition; Proper and Improper Ferroelectrics

Landau theory of phase transition is a phenomenological theory to describe the behavior of a system during a phase transition. In this theory, the energetics of the system near the phase transition is described by the *Landau free energy*  $F$ , which can be considered as an approximation to the Helmholtz or Gibbs free energy per unit volume. This Landau free energy can depend on external parameters like temperature, pressure, field, etc.

According to this theory, as the system is cooled from a disordered or higher symmetry state at high-temperature to an ordered state with reduced symmetry below the phase transition temperature  $T_c$ , a phenomenological order parameter  $\psi(T)$  takes a non-zero value below  $T_c$ . The main

Table 3: List of all the non-centrosymmetric crystal classes. The symbol (+) denotes the occurrence of that property and (-) shows the absence of the property. The symbol  $[u0w]$  refers to the set of directions obtained for all possible values of  $u$  and  $w$ , in this case to all directions normal to the  $b$  axis, i.e. parallel to the plane (010). Data adopted from reference [37].

Crystal System	Non-centrosymmetric Crystal Classes	Pyroelectricity	Piezoelectricity
Triclinic	1	$+ [uvw]$	+
Monoclinic	2	$+ [010]$	+
	$m$	$+ [u0w]$	+
Orthorhombic	222	-	+
	$mm2$	$+ [001]$	+
Tetragonal	4	$+ [001]$	+
	$\bar{4}$	-	+
	422	-	+
	$4mm$	$+ [001]$	+
	$\bar{4}2m$	-	+
Trigonal	3	$+ [001]$	+
	32	-	+
	$3m$	$+ [001]$	+
Hexagonal	6	$+ [001]$	+
	$\bar{6}$	-	+
	622	-	+
	$6mm$	$+ [001]$	+
	$\bar{6}2m$	-	+
Cubic	23	-	+
	432	-	-
	$\bar{4}3m$	-	+

concept in the Landau theory is that for a spatially uniform system the free energy is analytic in term is  $\psi$  and  $T$  and the free energy can be expanded in series of powers of the order parameter.

$$F = F_0 + \frac{a}{2}P^2 + \frac{b}{4}P^4 + \dots - EP \quad (38)$$

where  $E_0$  is the energy of the system above  $T_c$ ,  $E$  is the external bias electric field and the coefficients  $a, b, \dots$  are in general temperature dependent. The first coefficient  $a$  is considered to be linear function of temperature in the form  $a_0(T - T_0)$  where  $T_0$  is the Landau parameter temperature and may be equal or lower than the transition temperature. In order to find the value of  $P$  in thermal equilibrium, we need to minimize  $F$  as a function of  $P$ .

$$\frac{\partial F}{\partial P} = aP + bP^3 + \dots - E = 0 \quad (39)$$

If  $b > 0$  then a *second-order* phase transition takes place. Therefore polarization for zero applied field from Eq. 40 is found

$$a_0(T - T_0)P + bP^3 = 0 \quad (40)$$

so either  $P = 0$  or  $|P| = (a_0/b)^{1/2}(T_0 - T)^{1/2}$ . The temperature  $T_0$  in the second-order transition represent the Curie temperature. This transition is called second-order in a sense that the second derivative of the free energy (specific heat) is discontinuous and shows a divergence, while the first derivative is continuous at the critical point.

If  $b < 0$ , we will have a *first-order* phase transition. In this case a term of order six is needed in the Eq. 40 to keep the free energy positive. Therefore, in the absence of external field  $E$ , the

equilibrium condition can be written as

$$a_0(T - T_0)P - |b|P^3 + cP^5 = 0 \quad (41)$$

so either  $P = 0$  or

$$a_0(T - T_0) - |b|P^2 + cP^4 = 0 \quad (42)$$

This transition is called first-order in a sense that the first derivative of the free energy is discontinuous. Figure 7 shows the behavior of the free energy and polarization for the first- and second-order phase transition.

Ferroelectric materials for which the polarization is the primary order parameter is called *proper* ferroelectric and if the polarization is not the primary order parameter it is called *improper* ferroelectric.

One example of proper ferroelectricity is the barium titanate ( $\text{BaTiO}_3$ ) where the transition from the cubic to tetragonal phase is accompanied by a spontaneous deformation of the crystal. In this case the polarization is the order parameter as it accounts for the reduction in the symmetry, while the appearance of the spontaneous strain is a second-order effect and is a consequence of the polarization. If we polarize the cubic phase along a cubic edge, we obtain the tetragonal phase, even if the crystal is clamped. However, if the cubic phase is deformed, a tetragonal phase of higher symmetry will be achieved and the center of inversion is preserved [41].

In improper ferroelectrics, the polarization arises as a result of other changes in the crystal (or magnetic) structure of the material. Majority of magnetic ferroelectrics, in which the magnetic ordering breaks the inversion symmetry and induces a polarization are improper ferroelectrics.

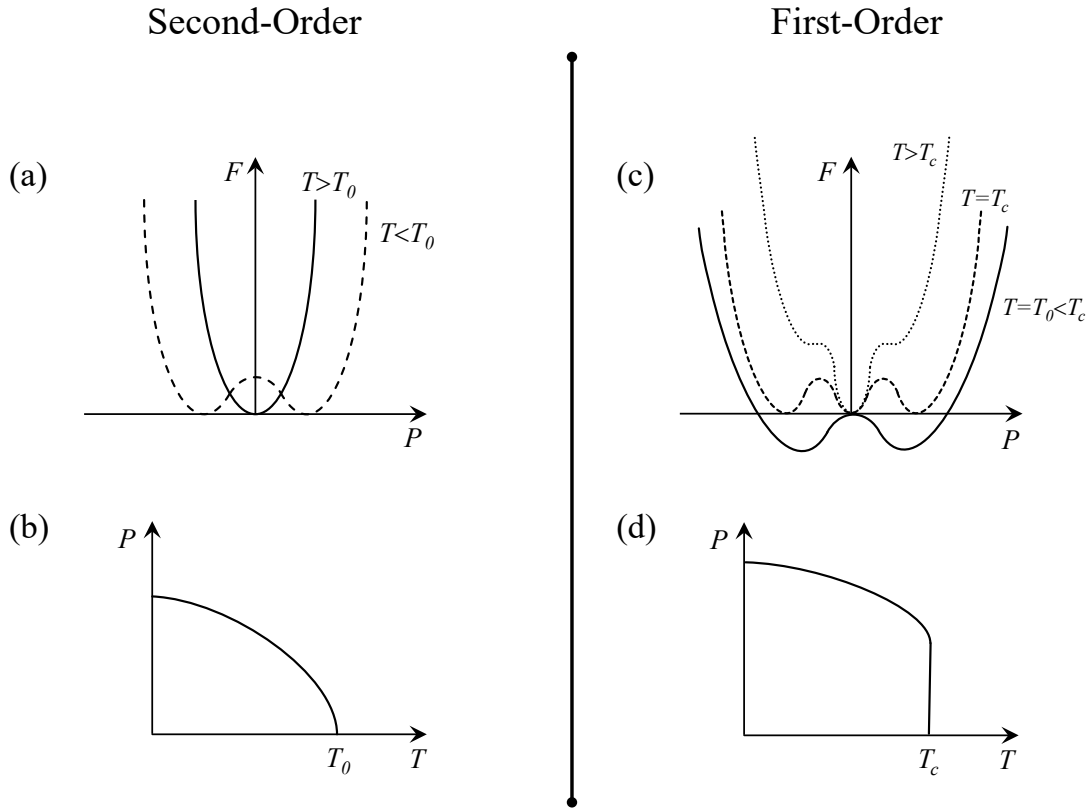


Figure 7: Second-order phase transition: (a) free energy as a function of order parameter  $P$  above and below the critical temperature and (b) order parameter  $P$  as a function of temperature. First-order phase transition: (c) free energy as a function of  $P$  for  $T < T_c$ ,  $T = T_c$ , and  $T > T_c$  and (d) the polarization  $P$  as a function of temperature.

## 2.7 Multiferroics

The combination of electricity and magnetism has been formulated in 19th century in the form of Maxwell equations. However, the electrically and magnetically ordered materials have been considered to be separate. In 1959, Landau and Lifshitz made a short remark in a volume of their Course of Theoretical Physics [42] regarding the possibility of linear coupling between magnetic and electric fields in a media, which would cause a magnetization proportional to an electric field. In 1959 Dzyaloshinskii [43] predicted the *magnetoelectric* coupling in antiferromagnet  $\text{Cr}_2\text{O}_3$  and Astrov [44] experimentally observed this effect.

Magnetoelectric (ME) coupling is the cross-coupling between the magnetic and electric response of the material where a magnetization  $\mathbf{M}$  can appear in the presence of an electric field  $\mathbf{E}$ , or the opposite effect, a polarization  $\mathbf{P}$  can appear in the presence of magnetic field  $\mathbf{H}$  [10, 11, 45, 46]. The ME coupling does not necessary requires the material to be ordered.

Extensive efforts were undertaken by Smolenskii and colleagues [1], to combine the magnetic and ferroelectric ordering in a single compound (formerly called *ferroelectromagnets*).

The term *multiferroic* was later coined by H. Schmid [47] for a material with two or more coexisting primary ferroic orders in a single phase of matter. The definitions has been broadened now to include coexistence of ferroelectricity with ferro-, ferri, and antiferromagnetic order in a single or multiphase of the compound. In general, multiferroic materials are categorized in two types: *type I* and *type II*.

When the origin of ferroelectricity and magnetic ordering are separate from each other the material is called type I multiferroic. In this class of multiferroics, the ferroelectricity usually emerges at high temperatures with a relatively large polarization (of order  $10 - 100 \mu\text{C}/\text{cm}^2$ ) and the magnetic ordering occurs at temperatures below room temperature. Due to separate origin of magnetic

ordering and ferroelectricity in type I multiferroics, the ME coupling is usually rather weak. Some of the well-known examples of type I multiferroics are the hexagonal rare-earth manganites  $h\text{-RMnO}_3$  (R=rare-earth) [8, 9, 14, 18] and  $\text{BiFeO}_3$  [48].

Unlike type I multiferroics, in type II the ferroelectricity and magnetic ordering have a unique origin. In this class of multiferroics, material develops a special form of magnetic ordering which breaks the inversion symmetry and as a result induces a ferroelectric polarization. The magnetic ordering in type II multiferroics usually occurs at temperatures far below room-temperature. Some of the well-known examples of multiferroics of spin origins are the  $\text{TbMnO}_3$  with orthorhombic structure and  $\text{TbMn}_2\text{O}_5$ . Due to the identical origin of ferroelectricity and magnetic ordering in type II multiferroics, the ME coupling is usually stronger in this class of materials.

## 2.8 Magnetoelectric Coupling and Mechanisms for Induced Polarization

The magnetoelectric coupling in a single phase material can be described by using the Landau theory of phase transition. By considering a medium which is both electrically and magnetically ordered (there is spontaneous polarization and magnetization), the free energy density can be written in the following form [11, 49–52]:

$$\begin{aligned}
 -\Phi(E, H, T) = & -\Phi_0 + E^i P_s^i(T) + H^i M_s^i(T) + \frac{1}{2} \epsilon_0 \epsilon_{ij}(T) E^i E^j + \frac{1}{2} \mu_0 \mu_{ij}(T) H^i H^j \\
 & + \frac{1}{2} \alpha_{ij}(T) E^i H^j + \frac{1}{2} \beta_{ijk} E^i H^j H^k + \frac{1}{2} \gamma_{ijk} H^i E^j E^k + \dots \quad (43)
 \end{aligned}$$

The  $i$ th component of total polarization  $P^i$  and total magnetization  $M^i$  can be found by taking derivative of the free energy with respect to electric field  $E^i$  and the magnetic field  $H^i$ , respectively:

$$\begin{aligned} P^i &= -\frac{\partial\Phi}{\partial E^i} = P_s^i + \epsilon_0\epsilon_{ij}(T)E^j + \alpha_{ij}(T)H^j + \frac{1}{2}\beta_{ijk}H^jH^k + \dots, \\ M^i &= -\frac{\partial\Phi}{\partial H^i} = M_s^i + \mu_0\mu_{ij}(T)H^j + \alpha_{ji}(T)H^j + \frac{1}{2}\gamma_{ijk}E^jE^k + \dots \end{aligned} \quad (44)$$

The first and second terms in Eq. 43 represent the contribution from the  $i$ th component of the spontaneous polarization and magnetization, respectively, where  $E^i$  denotes the  $i$ th component of applied electric field  $\mathbf{E}$  and  $H^i$  is the  $i$ th component of applied magnetic field  $\mathbf{H}$ . The third and fourth terms are the contribution from the electric and magnetic field, respectively, where  $\epsilon_0$  is the permittivity of free space,  $\epsilon_{ijk}$  is a second-rank tensor relative permittivity,  $\mu_0$  is the permeability of free space, and  $\mu_{ij}(T)$  is the relative permeability. The fifth term describes the magnetoelectric coupling via  $\alpha_{ijk}$ . The  $\beta_{ijk}$  and  $\gamma_{ijk}$  are the third-rank tensor representing the second-order (quadratic) ME coupling. The indices follow the Einstein summation convention so they run from 1 to 3.

It is worth mentioning that the free energy can also be written in the form of Landau free energy in the following form [1, 41, 53]

$$\Phi = \Phi_0 + \alpha P^2 + \frac{\beta}{2}P^4 - PE + \alpha' M^2 + \frac{\beta'}{2}M^4 - MH + \gamma P^2 M^2 \quad (45)$$

where  $M$  and  $P$  are the magnetization and polarization, respectively, and  $\Phi, \alpha, \beta, \alpha', \beta'$  and  $\gamma$  are all temperature-dependent. The term  $\gamma P^2 M^2$  signifies the coupling between the polarization and magnetization.

The spin-driven polarization in type II multiferroics can emerge through different mechanisms.

There are essentially three mechanisms, which can break the inversion symmetry in a material and induce a polarization [45, 46, 54, 55]: (i) anti-symmetric spin exchange interaction, (ii) symmetric spin exchange interaction, and (iii) spin-ligand interaction (or spin-dependent  $p$ - $d$  hybridization).

The anti-symmetric spin exchange interaction can explain the induced polarization between adjacent canted spins, as depicted in Fig. 8 and it is proportional to the cross product of spins in the following form:

$$\mathbf{P}_{ij} \propto \mathbf{e}_{ij} \times (\mathbf{S}_i \times \mathbf{S}_j), \quad (46)$$

where  $\mathbf{S}_i$  and  $\mathbf{S}_j$  are the neighboring canted spins,  $\mathbf{e}_{ij}$  is the unit vector connecting the two spins, and  $\mathbf{P}_{ij}$  is the local polarization between the  $i$ th and  $j$ th sites.

In special magnetic structures like cycloidal or transverse conical the local polarization can rise to a macroscopic polarization.

A microscopic theory by (Katsura–Nagaosa–Balatsky) [3] explain the origin of this polarization by considering a spontaneous flow of *spin-current* between canted spins, which generates a polarization under the influence of *spin-orbit* interaction. This mechanism is also called inverse Dzyaloshinskii–Moriya (DM) model [56] since in the conventional DM interaction a non-centrosymmetric crystallographic environment promotes an antisymmetric magnetic interaction (canting of spins) and, conversely, in the inverse DM interaction a canted spin structure drives a non-centrosymmetric displacement of charges. Spin-orbit coupling is crucial for both the DM and inverse DM interaction.

The symmetric spin exchange model is based on the fact that two different types of bonds results in changes in the bond lengths and angles due to *exchange striction* (i.e., difference in interatomic forces), which may induce a polar striction along bond length (Fig. 9). This model essentially

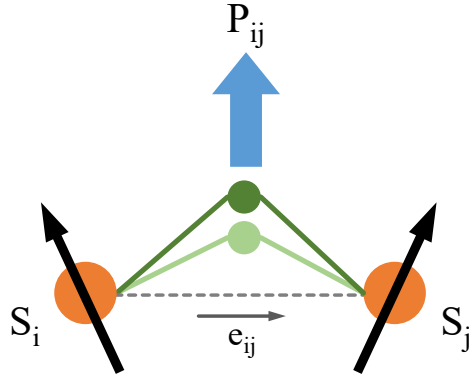


Figure 8: Local polarization  $P_{ij}$  generated between canted adjacent spins  $S_i$  and  $S_j$ . The anti-symmetric exchange interaction causes the displacement of ligand cation (green circle) with respect to magnetic ions (orange circles), which induces a polarization in vertical direction (blue arrow).

convey the *spin-lattice coupling* in the system. The polarization induced according to this model has the following form:

$$\mathbf{P}_{ij} \propto \mathbf{\Pi}_{ij}(\mathbf{S}_i \cdot \mathbf{S}_j), \quad (47)$$

where  $\mathbf{S}_i$  and  $\mathbf{S}_j$  are the neighboring canted spins, and  $\mathbf{\Pi}_{ij}$  is the specific crystallographic direction along which the striction occurs, and  $\mathbf{P}_{ij}$  is the local polarization between the  $i$ th and  $j$ th sites. The polarization induced by this model can, in principle, be larger than those generated by the anti-symmetric exchange model. This is because the polarization generated by this mechanism depends on the exchange striction, which can be stronger than the weak spin-orbit coupling, which is required by the anti-symmetric exchange mechanism.

In the spin-ligand interaction mechanism the locally polar bond between a magnetic  $d$  orbital and a ligand  $p$  orbital can be modulated by a spin-dependent hybridization due to relativistic

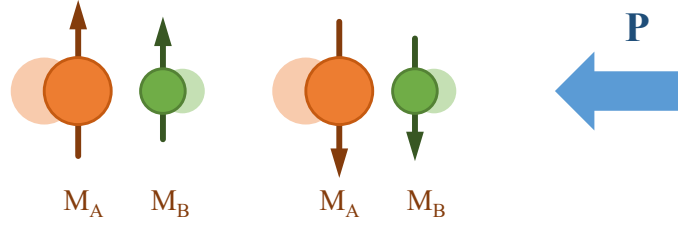


Figure 9: Polarization  $\mathbf{P}$  generated by exchange interaction between two magnetic ions  $M_A$  and  $M_B$ .

spin-orbit coupling, which results in a local polarization of the following form:

$$\mathbf{P}_{il} \propto (\mathbf{S}_i \cdot \mathbf{e}_{il})^2 \mathbf{e}_{il}, \quad (48)$$

Under certain crystallographic lattice (e.g.,  $MX_4$  tetrahedra with  $M$  being magnetic ion and  $X$  the ligand) the sum over the crystal structure does not cancel and a macroscopic polarization  $\mathbf{P}$  will arise

The ME coupling in type II multiferroics can mediate through different mechanisms, which in essence, is in direct relation with the origin of polarization. Some of these mechanisms as mentioned are: spin-orbit coupling, spin-lattice coupling, and spin-charge coupling.

## 3 Methods and Experiments

In this chapter the experimental techniques and instruments that were used in this study is explained. We begin by explaining the process for synthesizing the samples and the sample characterization by X-ray diffraction and X-ray absorption spectroscopy. We will give special attention to dielectric, pyrocurrent, and polarization measurement. At the end the method used in measuring the heat capacity is explained.

### 3.1 Sample Preparation

Polycrystalline samples of  $RFeWO_6$  ( $R=Ho, Dy, \text{ and } Tb$ ) were prepared using a conventional solid-state reaction method. In this synthesis route a mixture of fine powders of precursors are heated at a relatively high temperature. This allows the chemical reaction between reactants by solid-state diffusion of the ions, which is characterized by a slow kinetic rate. For the reaction to occur in a reasonable time, the Tamman's rule can be followed, which suggests a synthesis temperature of about two-thirds of the lowest melting point of the reactants.

The synthesis of these compounds was done in two steps. To avoid the formation of  $Fe_3O_4$  at high temperature, rare-earth orthoferrites were synthesized first and then they were mixed with Tungstate [31].

To synthesize  $RFeO_3$  ( $R=Ho, Dy, \text{ and } Tb$ ), stoichiometric amounts of precursors  $R_2O_3$  ( $R=Ho$  and  $Dy$ ) and  $Tb_4O_7$  were mixed, separately, with  $Fe_2O_3$  and ground thoroughly and pressed into pellets. Before mixing the precursors the rare-earth oxides were preheated at  $900\text{ }^\circ\text{C}$  inside a tube furnace overnight. The crucible containing the rare-earth oxide was then removed from the furnace, while still hot, and was placed in a desiccator and vacuumed to cool down. The pellets were then treated at the final temperature of  $1350\text{ }^\circ\text{C}$  overnight with several intermittent grindings. The

sintering temperature for each session of grinding/pelletization/sintering was increased gradually to reach the final temperature. The quality of rare-earth orthoferrites was checked with XRD and after confirming the phase purity, in the second step, it was then mixed with  $\text{WO}_3$  in stoichiometric ratio. The mixture was pelletized and treated at the final temperature of 1050 °C for the case of Ho, 1020 °C for Dy, and 1060 °C for the case of Tb overnight in Argon flow with intermittent grindings. Synthesis in air was tried for the second step but we could not get the desired phase.

All the synthesis process described were performed at Texas Center for Superconductivity (TcSUH). The final products were ground for synchrotron XRD measurements. Part of the powder was pressed into pellets of appropriate size and shape and then sintered in furnace for dielectric, polarization, magnetic and heat capacity measurements.

### **3.2 X-ray Diffraction and Rietveld Refinement**

To ensure the quality of the samples studied in this thesis and characterize the crystal structure, powder X-ray diffraction (XRD) was collected from samples. During the synthesis, to check the quality of precursors and the progress of synthesis, laboratory XRD patterns were collected at the Material Characterization Facility at TcSUH, using a RIGAKU SmartLab machine. The XRD patterns were indexed using the qualitative analysis, the so-called search/match method, in which the measured pattern is compared with a database to find out the phases of the sample. After ensuring the phase purity of the final product at TcSUH, synchrotron XRD patterns at low- and room-temperature were collected at National Synchrotron Radiation Research Center at Taiwan by our collaborator Chung-Kai Chang and Yen-Chung Lai, for quantitative analysis. The quantitative analysis and Rietveld Refinement were performed at TcSUH using the software GSAS-II [57].

### 3.3 X-ray Absorption Spectroscopy and X-ray Magnetic Circular Dichroism Spectroscopy

The synchrotron soft X-ray absorption spectroscopy (XAS) and soft X-ray magnetic circular dichroism (XMCD) were performed at the BOREAS beamline of the ALBA Synchrotron Light Facility [58] with the collaboration of ALBA staff. Since these compounds are strong insulators, powder samples of  $\text{RFeWO}_6$  (R=Ho, Dy, and Tb) were mixed thoroughly with pure gold powder (with a ratio of  $\sim 4 : 1$ ) and pressed into pellets and sintered at  $\sim 900$  °C. The samples were prepared in Tc-SUH and the data acquisition and analysis were performed by Dr. Stefano Agrestini, Dr. Javier Herrero-Martin, Dr. José Luis García-Muñoz, and Dr. Eric Pellegrin.

### 3.4 Density Functional Theory (DFT) Calculations

The unit cell provided by XRD measurement at 300 K was used for the density functional theory (DFT) calculations. The stoichiometric unit cell contains 36 atoms: 4 Ho, 4 W, 4 Fe, and 24 O atoms. All periodic, spin-polarized DFT calculations were carried out using the Vienna *ab initio* simulation package (VASP) [59–61] version 5.4.1 and the atomic simulation environment (ASE) [62]. Exchange and correlation effects were taken into account using the PBE density functional introduced by Perdew, Burke, and Ernzerhof [63]. The wave function of the valence electrons was expanded into a plane wave basis set with an energy cutoff of 400 eV, while the core electrons were represented using the projector augmented wave function (PAW) method [64, 65]. Given the size of the simulation box, a  $\Gamma$ -centered (2, 4, 3)  $k$ -point grid was considered for sampling the reciprocal space. A Gaussian-smearing scheme with  $k_B T = 0.2$  eV was used to treat discontinuities at the Fermi level, and the total energy was extrapolated to  $k_B T = 0.0$  eV. Self-consistent field calculations were performed until a determination of energy accuracy to  $10^{-5}$  eV was achieved.

Geometry optimizations were performed with the conjugate-gradient algorithm until the maximum force acting on atoms was less than  $0.02 \text{ eV}/\text{\AA}$ . To include exact exchange effects, which are known to be able to widen the bandgap and provide a better density of states and band structure, the HSE06 hybrid density functional [66] was employed for single-point wave function calculations. The electronic properties of the system were obtained from the HSE06 wave function.

The DFT calculations and the analysis were performed by Dr. Taha Salavati-fard and Dr. Lars C. Grabow at TcSUH and William A. Brookshire Department of Chemical and Biomolecular Engineering, University of Houston.

### **3.5 Magnetic Property**

The magnetic properties of the compounds were studied at TcSUH by measuring the DC and AC magnetization over a range of temperature 2 K–300 K and magnetic field up to 7 T. For this purpose a SQUID magnetometer, Magnetic Property Measurement System (MPMS3) by Quantum Design was used. MPMS3 is equipped with a superconducting magnet, which can generate a static or an oscillating magnetic field and a superconducting pickup coil and the SQUID amplifier, which is capable of detecting extremely small magnetic signal.

### **3.6 Physical Property Measurement System**

Physical Property Measurement System (PPMS) by Quantum Design was used for dielectric constant, pyrocurrent, and heat capacity measurements. The PPMS allows one to control the temperature in a range of 1.9 K–400 K and under an applied magnetic field up to 7 T that is produced by a superconducting magnet.

### 3.7 Dielectric Constant

Since the PPMS is not equipped with internal shielded wires, which is essential for high-precision dielectric measurements, we used a home built, top-loaded, low temperature capacitance probe for dielectric and pyrocurrent measurements. The wires used inside the probe are shielded coaxial wires suitable for low-temperature measurements. The dielectric constant of the sample is found by measuring the capacitance of the sample that is made into a parallel-plate capacitor. For this purpose both faces of a thin, disk-shape piece of sample is covered by silver paint to serve as electrodes. Thin Pt wires are then attached to each face. The sample is mounted on the probe by placing it on a thin piece of G-10 (an epoxy composite) and with the help of GE-varnish (an insulating adhesive). The Pt wires are then soldered to the capacitance probe. To measure the capacitance the Andeen-Hagerling (AH2500a) ultra-precision capacitance bridge, which operates with an excitation of up to 15 V rms at a fixed frequency of 1 kHz was used. The capacitance bridges reports the capacitance and the imaginary part of the dielectric constant ( $\text{Tan}\delta$  or loss tangent), which represents the energy loss. By assuming that the sample is an ideal parallel-plate capacitor, the dielectric constant is given by

$$\epsilon_r = \frac{Cd}{\epsilon_0 A} \quad (49)$$

where  $C$  is the capacitance of the sample,  $d$  is the sample thickness, and  $A$  is the surface area of the sample. The temperature control and the external magnetic field was provided by the PPMS. To measure the temperature-dependent capacitance under different magnetic field, capacitance was measured during both cooling and warming at the rate 1–2 K/min to ensure that sample is always at thermal equilibrium.

### 3.8 Pyroelectric Current and Polarization Measurement

To measure the electric polarization as a function of temperature,  $\Delta P(T)$ , temperature-dependent pyroelectric current or pyrocurrent,  $I_p(T)$ , was measured by using a Keithley electrometer (K6517A). To measure  $I_p(T)$  we used the same experimental setup and sample preparation procedures that was used for capacitance measurement, as described in section 3.7. A poling electric field,  $E_{\text{pole}}$ , was applied to the sample at a temperature (a few Kelvin) above the transition temperature and then sample was cooled to the lowest temperature of 2 K.  $E_{\text{pole}}$  was then removed at the 2 K, the desired magnetic field was applied, and  $I_p(T)$  was recorded when the sample was warming up with a rate 2 – 3 K/min. The  $E_{\text{pole}}$  makes the electric dipoles that are formed in the ferroelectric phase to line up with field and allows it be measured as  $I_p$  when the sample is warmed up. The poling voltage we used is typically 80 V–140 V corresponding to an electric field of 100 kV/m–270 kV/m inside the sample. Measurements were performed with reverse bias field to ensure that the observed polarization can be switched by field. Polarization is found by integrating the  $I_p$  in time as shown below:

$$P = \frac{Q}{A} \quad (50)$$

therefore

$$\begin{aligned} \frac{dP}{dT} &= \frac{1}{A} \frac{dQ}{dT} = \frac{1}{A} \frac{dt}{dT} \frac{dQ}{dt} \\ &= \frac{1}{A} \frac{dt}{dT} I_p \end{aligned} \quad (51)$$

and as a results

$$P(t) = \frac{1}{A} \int_{t'=0}^{t'=t} I_p(t') dt' \quad (52)$$

During the data acquisition pyrocurrent, temperature, and time are recorded and since the temperature is changed with a constant rate, the integration in time can be converted to temperature ( $t = t(T) \rightarrow P(T)$ ).

### 3.9 Specific Heat

To characterize the thermodynamic properties and the phase transition of the samples of our study, the heat capacity at constant pressure and as a function of temperature,  $C_p(T)$ , under different magnetic field was measured. The  $C_p(T)$  was measured by the relaxation technique using the Quantum Design Heat Capacity option in PPMS and the standard heat capacity puck (Fig. 10) by Quantum Design.

The measurement was performed in the temperature range 1.9 K–300 K and an applied field of up to 7 T. The samples used for the measurements had a flat surface and a mass of  $\sim 3$  mg. The sample is mounted on the sample platform using Apiezon N grease. Small wires connect the sample platform to the puck, which provides electrical connection to the heater and thermometer at the bottom side of the platform. These wires also serve as structural support for the platform. The wires that connect the sample platform to the puck frame create a well-controlled connection with the thermal bath. The pressure inside the probe is kept less than approximately 1 mTorr, using the high-vacuum system, to eliminate alternate thermal links through residual gas.

Before the specific heat of the sample is measured, the heat capacity contribution by the N grease used for sample contact (called addenda) should be measured first. During the heat capacity measurement a known amount of heat is applied to the sample at constant power for a fixed amount of time, which is followed by a cooling period of the same duration. The entire temperature response

of the sample platform is then fit with a simple model using the following equation:

$$C_{total} \frac{dT}{dt} = -K_w(T - T_b) + P(t), \quad (53)$$

where  $C_{total}$  is the total heat capacity of the sample and sample platform,  $K_w$  is the thermal conductance of the supporting wires,  $T_b$  is the temperature of the thermal bath (puck frame), and  $P(t)$  is the power applied by the heater. The heater power  $P(t)$  is equal to  $P_0$  during the heating portion of the measurement and equal to zero during the cooling portion. The solution of Eq. 53 is an exponential function with a characteristic time constant  $\tau$  equal to  $C_{total}/K$ .

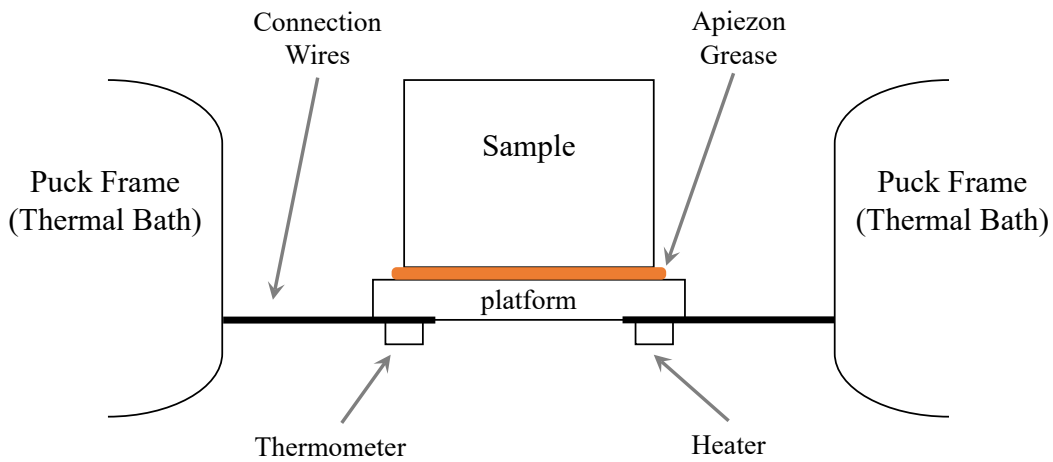


Figure 10: Thermal connection between sample and sample platform in the PPMS Heat Capacity Option [67].

## 4 Results and Discussion

This chapter is dedicated to discuss the experimental and computational results on multiferroic properties of  $\text{RFeWO}_6$  ( $\text{R} = \text{Ho, Dy, and Tb}$ ) and in particular, the magnetocapacitance and magnetoelectric coupling in these compounds.

The content of this chapter is mainly adopted from the following published paper:

**M. Adnani**, M. Gooch, L. Deng, S. Agrestini, J. Herrero-Martin, H.-C. Wu, C.-K. Chang, T. Salavati-fard, N. Poudel, J. L. García-Muñoz, S. Daneshmandi, Z. Wu, L. C. Grabow, Y.-C. Lai, H.-D. Yang, E. Pellegrin, and C.-W. Chu, *Magnetocapacitance effect and magnetoelectric coupling in type-II multiferroic  $\text{HoFeWO}_6$* , Phys. Rev. B **103**, 094110 (2021).

### 4.1 Crystal Structure of $\text{RFeWO}_6$ ( $\text{R} = \text{Ho, Dy, and Tb}$ )

The quality of precursors and final products were checked by laboratory XRD during the synthesis. The XRD pattern for  $\text{HoFeWO}_6$  was measured at synchrotron facility at National Synchrotron Radiation Research Center at Taiwan. Rietveld refinement was performed on synchrotron XRD pattern of  $\text{HoFeWO}_6$  collected at room-temperature at TcSUH to obtain the crystal structure parameters and atomic positions. By using the standard orthorhombic space group  $Pna2_1$  (no. 33) we were able to index and fit all the peaks. A few tiny extra peaks were also observed but we could not index or identify them. These peaks are likely due to small amount of impurity phase. Figure 11 shows the measured XRD pattern and the calculated profile for  $\text{HoFeWO}_6$ . The measured XRD pattern and the calculated profile is also plotted in the logarithmic scale in Fig. 12. The results of the refinement including lattice parameters and the atomic positions are summarized in Table 4.

Room-temperature XRD patterns of  $\text{DyFeWO}_6$  and  $\text{TbFeWO}_6$  were also collected at TcSUH and all the peaks were indexed by using the space group  $Pna2_1$ , however, Rietveld refinement was

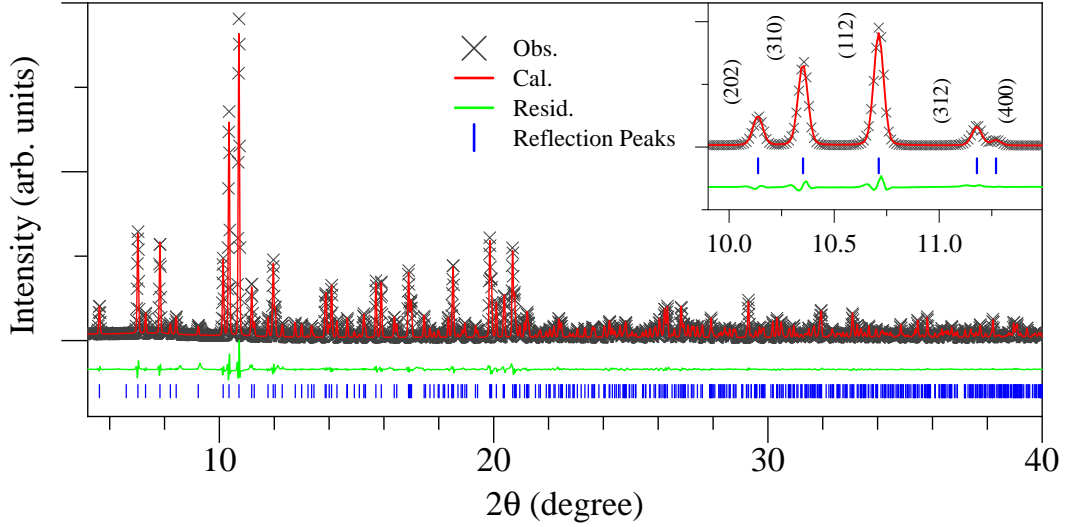


Figure 11: Rietveld refinement of the room-temperature synchrotron XRD data for  $\text{HoFeWO}_6$ . Crosses: measurement data; red solid line: calculated profile; green solid line: the difference between the observation and the calculated profile; and vertical bars: positions of Bragg peaks. Inset: magnified view of the main peaks.

not performed on these patterns. Small number of tiny peaks were visible in the patterns which could not be indexed or identified. Figure 13 shows the lab XRD pattern for  $\text{HoFeWO}_6$ ,  $\text{DyFeWO}_6$ ,  $\text{TbFeWO}_6$ , and the Bragg reflection peaks for space group  $Pna2_1$ .

These compounds with an aeschynite-type crystal structure and a general formula of  $\text{RMM}'\text{O}_6$  (R=rare-earth; M, M'=transition metals) will adopt a polar structure, due to symmetry constraints, if M and M' have an ordered arrangements [30]. Salmon *et.al* [31] reported that  $\text{RMWO}_6$  (R=rare-earth; M=Fe, Cr, and V) have an ordered arrangement of  $\text{M}^{+3}$  and  $\text{W}^{+6}$  and that they show an AFM ordering at low temperature. Figure 14 shows a view of crystal structure of  $\text{HoFeWO}_6$ , as an example, in different orientations. The crystal structure of these compounds is consists of edge-sharing octahedra of  $\text{FeO}_6$  and  $\text{WO}_6$ , forming a dimer. The dimers are connected corner-sharing to create a three-dimensional structure with  $\text{R}^{3+}$  ions located in the channels in between the  $\text{Fe}^{+3}$  and  $\text{W}^{+6}$  octahedra. This can be seen in Fig. 15.

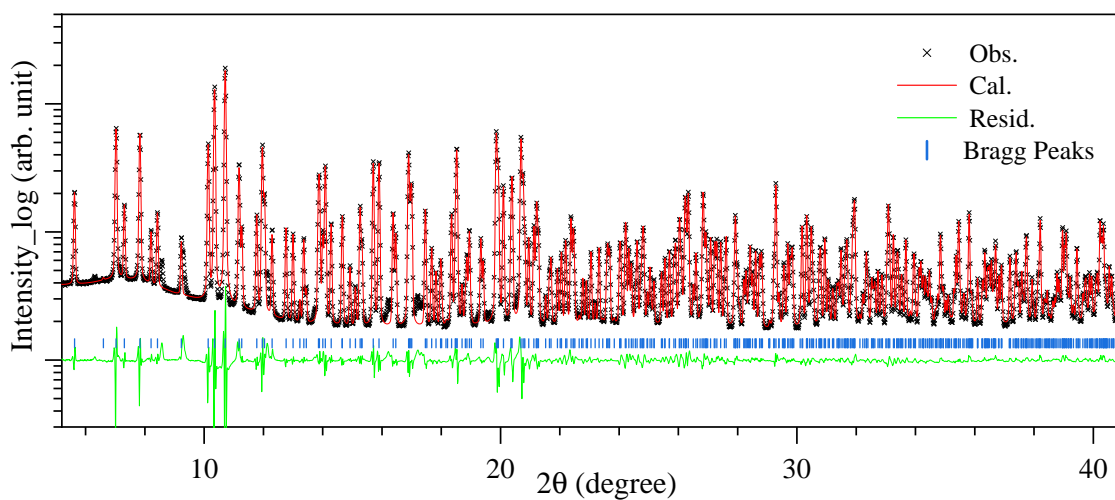


Figure 12: Room-temperature synchrotron XRD pattern for  $\text{HoFeWO}_6$  and the Rietveld refinement in logarithmic scale. Crosses: measurement data; red solid line: calculated profile; green solid line: the difference between the observation and the calculated profile; and vertical bars: positions of Bragg peaks.

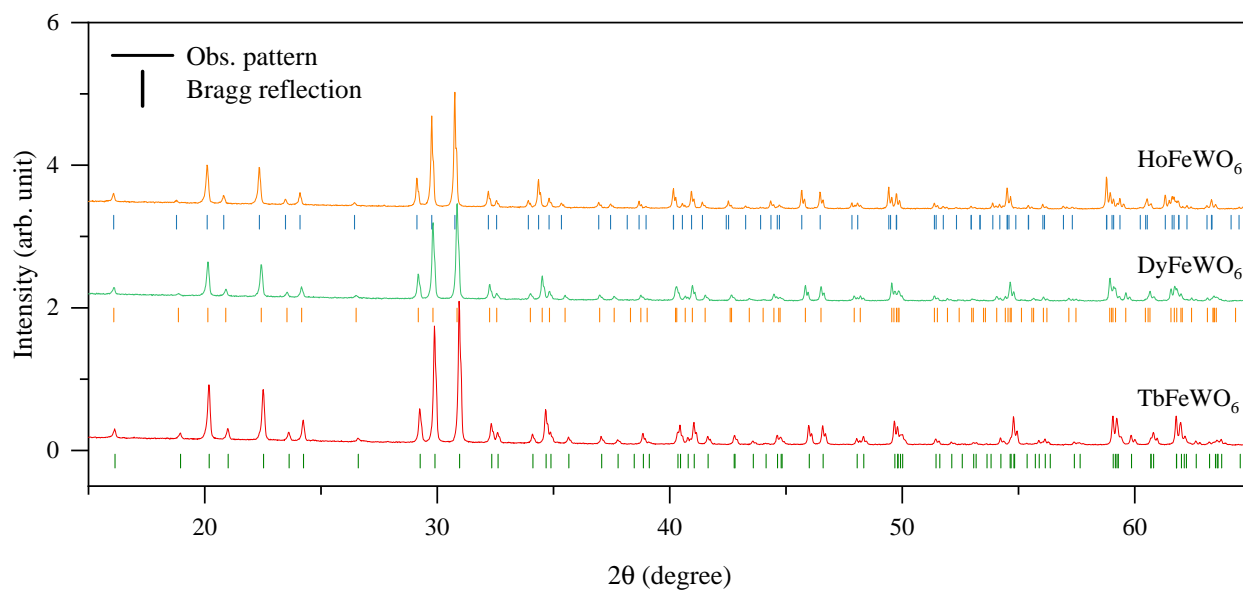


Figure 13: Room-temperature laboratory XRD pattern for  $\text{HoFeWO}_6$ ,  $\text{DyFeWO}_6$ , and  $\text{TbFeWO}_6$ . Solid line: measured profile; and vertical bars: Bragg peaks.

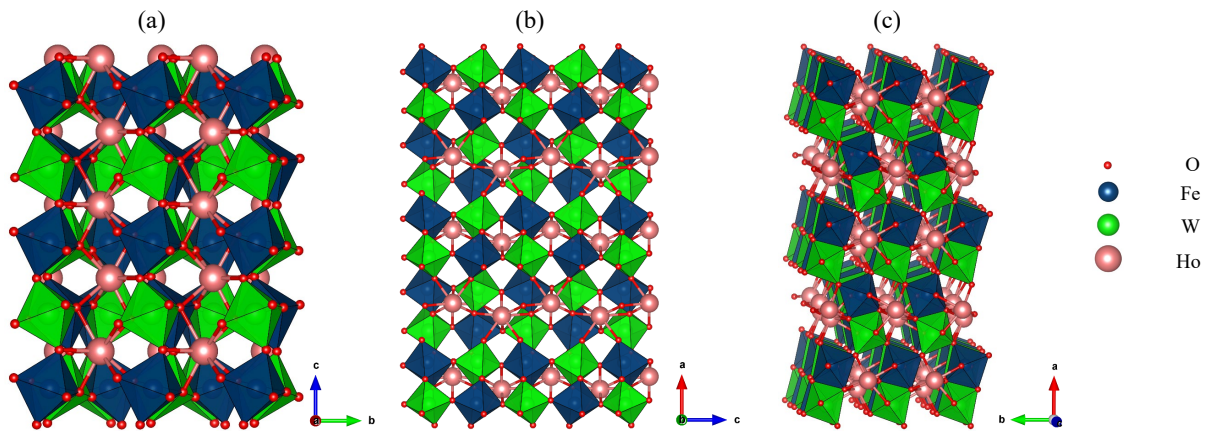


Figure 14: (a)-(c) Views of the crystal structure of  $\text{HoFeWO}_6$  in different orientations.

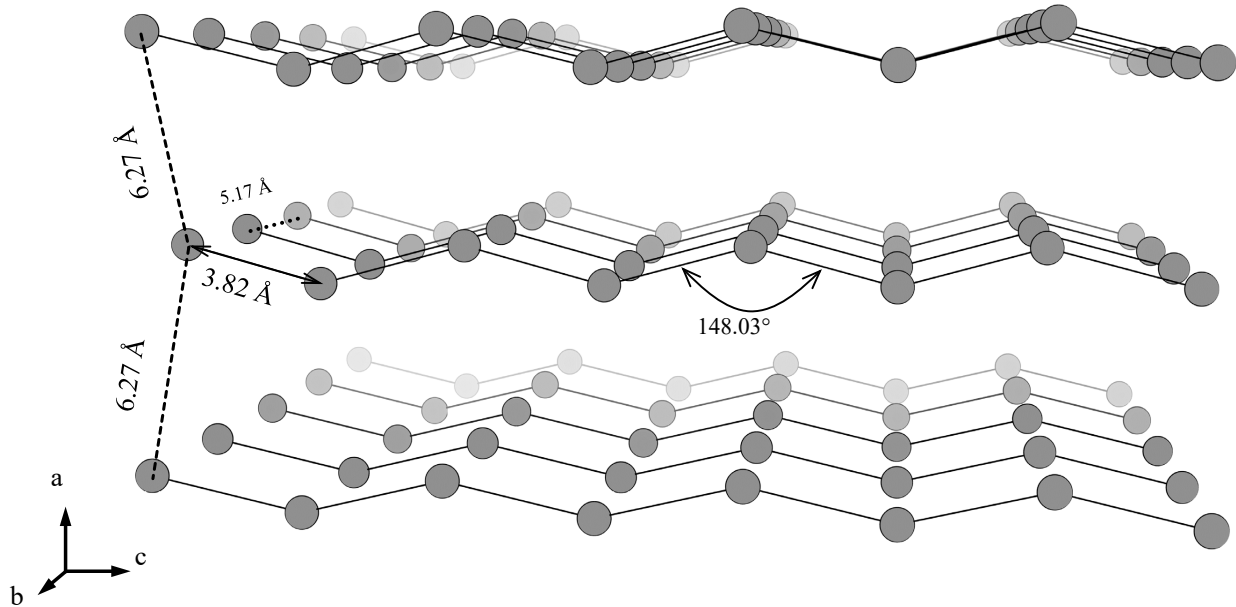


Figure 15:  $\text{Ho}^{3+}$  ions occupy the channels in between the octahedra, forming a quasi-one-dimensional chain along the  $c$  direction. The figure shows a schematics of  $\text{Ho}^{3+}$  ions with appropriate dimensions.

Table 4: Structural and lattice parameters of HoFeWO<sub>6</sub> obtained from the Rietveld refinement of XRD data at T = 300 K.

Atom	x	y	z	Occupancy	U <sub>iso</sub> (Å <sup>2</sup> )	site
Ho	0.0430(1)	0.4564(3)	0.2476(5)	1	0.0179(3)	4a
Fe	0.1393(5)	0.9633(9)	0.9907(14)	1	0.015(1)	4a
W	0.3544(2)	0.4517(3)	0.00350(15)	1	0.0181(3)	4a
O1	0.966(2)	0.780(4)	0.047(4)	1	0.018(2)	4a
O2	0.521(2)	0.250(4)	0.966(4)	1	0.018(2)	4a
O3	0.217(2)	0.611(4)	0.061(3)	1	0.018(2)	4a
O4	0.297(2)	0.135(5)	0.933(3)	1	0.018(2)	4a
O5	0.145(2)	0.060(4)	0.263(3)	1	0.018(2)	4a
O6	0.118(2)	0.836(4)	0.742(5)	1	0.018(2)	4a

Space group= $Pna2_1$ ; Lattice parameters:  $a = 10.973(1)\text{\AA}$ ,  $b = 5.1696(5)\text{\AA}$ ,  $c = 7.3342(6)\text{\AA}$ ;  
 $\alpha = \beta = \gamma = 90^\circ$ ; Volume =  $416.046(5)\text{\AA}^3$ ;  
 $R_F = 3.24\%$ ,  $R_F^2 = 4.64$ ,  $wR = 8.61\%$ ,  $R = 6.35\%$ ,  $\chi^2 = 2.12$

We performed low-temperature XRD on powder sample of HoFeWO<sub>6</sub> from 30–8 K and sequential Rietveld refinement was performed on the patterns. The quality and resolution of low-temperature XRD patterns were not adequate and therefore the Rietveld refinement did not give a good fit. Figure 16 shows the XRD pattern at 30 and 8 K and the Bragg reflections corresponding to space group  $Pna2_1$ . All the peaks can be matched with the Bragg reflections of  $Pna2_1$  and therefore we can conclude the absence of structural phase transition for this temperature range. Neutron diffraction measurement on DyFeWO<sub>6</sub> at 3.5 K also showed no sign of structural phase transition [28]. Our structural relaxation calculation by the PBE density functional on HoFeWO<sub>6</sub> also revealed no structural transition for this compound, therefore the space group  $Pna2_1$  is the stable structure for this compounds. Table 5 compares the lattice parameters from XRD at T=300 K and 8 K and from density functional theory (DFT) calculations with each other.

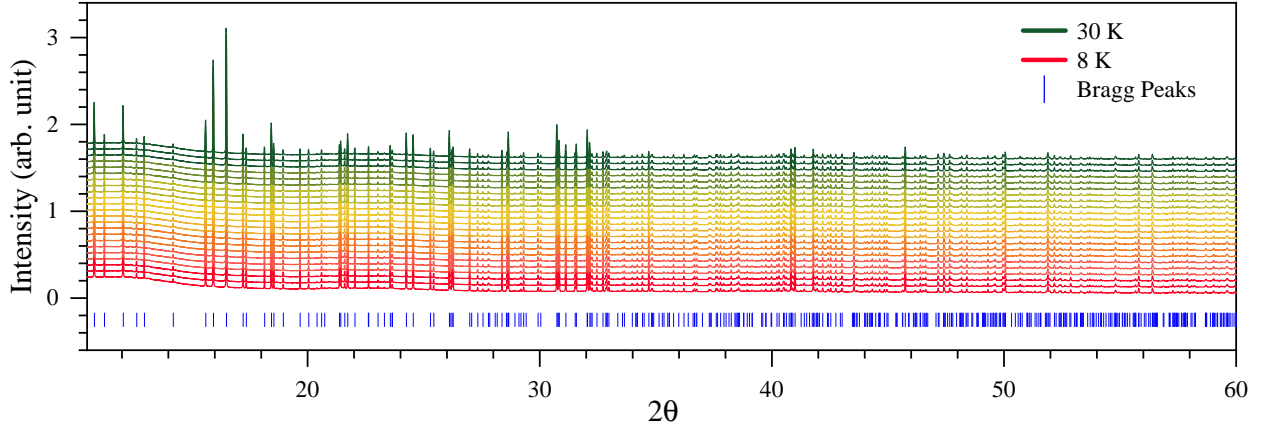


Figure 16: Low temperature XRD pattern of  $\text{HoFeWO}_6$  from 30–8 K and the Bragg reflections corresponding to the space group  $Pna2_1$ .

Table 5: Lattice parameters obtained from XRD at  $T = 300$  K and  $T = 8$  K and from DFT calculations.

	a (Å)	b (Å)	c (Å)	Vol. (Å <sup>3</sup> )
XRD (300 K)	10.973(1)	5.1696(5)	7.3342(6)	416.05(5)
XRD (8 K)	10.9537(4)	5.1574(2)	7.31892(23)	413.463(2)
DFT	10.99	5.15	7.31	413.88

## 4.2 X-ray absorption spectroscopy (XAS) and X-ray magnetic circular dichroism (XMCD) Results on $\text{RFeWO}_6$ (R = Ho, Dy, and Tb)

In order to investigate the oxidation state of Fe and rare-earth cations in  $\text{RFeWO}_6$  (R=Ho, Dy, and Tb) samples we made use of X-ray absorption spectroscopy (XAS) and X-ray magnetic circular dichroism (XMCD). As mentioned in Ch. 3.3 the samples used for XAS and XMCD measurements were prepared at TcSUH and the data acquisition and analysis were performed at ALBA. The X-ray absorption spectra are collected by using a circularly polarized light with the photon spin aligned parallel ( $\sigma^+$ ) and antiparallel ( $\sigma^-$ ) to the magnetic field. In this case the difference spectrum ( $\sigma^+ - \sigma^-$ ) is called XMCD and the sum spectrum ( $\sigma^+ + \sigma^-$ ) is called XAS. The energy position of XAS white lines increases systematically with the valence state of the ion [68–71], which makes

this method suitable to probe the valence state of compounds.

Figure 17 shows the Fe  $L_{2,3}$  XAS and XMCD for  $R\text{FeWO}_6$  ( $R=\text{Ho}$ ,  $\text{Dy}$ , and  $\text{Tb}$ ) samples, collected under at 2 K and under magnetic field of 6 T. In figure 17(a) XAS spectrum of  $\alpha - \text{Fe}_2\text{O}_3$  as a  $\text{Fe}^{3+}$  high spin  $S = 5/2$  is presented as a reference sample. The energy position of XAS white lines of our samples is similar to that of  $\alpha - \text{Fe}_2\text{O}_3$ , which demonstrates that the valence state of Fe is  $3+$  in  $R\text{FeWO}_6$  ( $R=\text{Ho}$ ,  $\text{Dy}$ , and  $\text{Tb}$ ).

Both the XAS and XMCD spectra exhibit a complex lineshape called multiplet structure, which depends on the multiplet interaction, the crystal field and the hybridization, and as such is very sensitive to the symmetry of the electronic and magnetic ground states. The fact that the lineshape of the XAS and XMCD spectra is practically identical for all three samples suggests a common ground state. The multiplet features of XAS are very similar to those of  $\alpha - \text{Fe}_2\text{O}_3$  demonstrates that the  $\text{Fe}^{3+}$  ions in  $R\text{FeWO}_6$  ( $R=\text{Ho}$ ,  $\text{Dy}$ , and  $\text{Tb}$ ) have a high spin  $S = 5/2$  state. In spite of the large spin moment, the measured Fe  $L_{2,3}$  XMCD signal is only 2.5 – 5% of the intensity of XAS. In Fig. 17(b-d) a scale factor of 10 was applied for a better view of the spectra. The spin and orbital moments were obtained from the XMCD data by using the sum rules for XMCD developed by Thole *et al.* [72] and Carra *et al.* [73]. The details of the calculations are mentioned in [74]. The results of the application of the sum rules are presented in Table 6. The net magnetic moment of the  $\text{Fe}^{3+}$  ion ( $m_s + m_l$ ) at the temperature of 2 K and under an applied field of 6 T is about 0.27, 0.48, and 0.52  $\mu_B/\text{ion}$  for the  $R = \text{Ho}$ ,  $\text{Dy}$  and  $\text{Tb}$  samples, respectively. This value is much smaller than the saturated moment of 5  $\mu_B$ , as well as the paramagnetic moment of 4.4  $\mu_B$  in  $\text{Fe}^{3+}$  estimated for  $T = 2$  K and  $B = 6$  T considering a Boltzmann population of the many-body energy levels. Such a small moment rules out either a ferromagnetic or a paramagnetic ground states and suggests an AFM ordering of the  $\text{Fe}^{3+}$  moments.

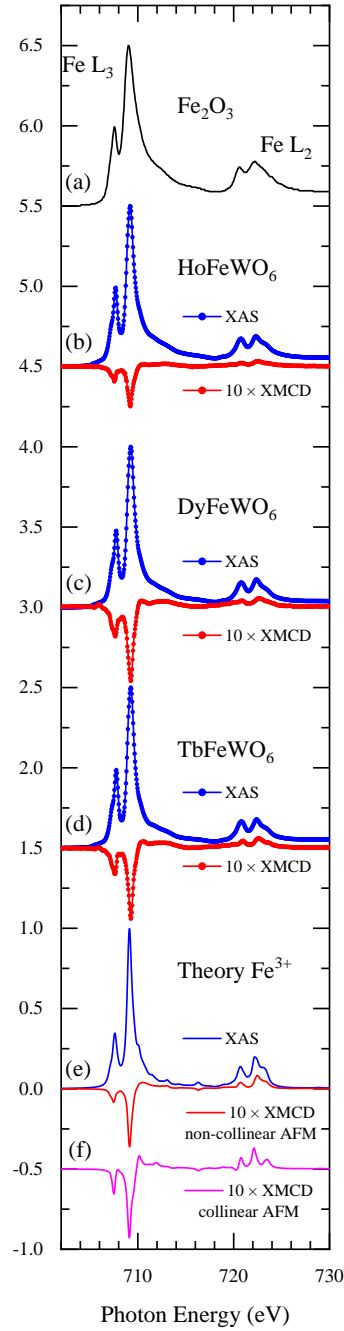


Figure 17: (a) Fe  $L_{2,3}$  XAS spectrum of  $\text{Fe}_2\text{O}_3$ . Fe  $L_{2,3}$  XAS (blue) and XMCD (red) spectra of  $\text{RFeWO}_6$  for  $\text{R} = \text{Ho}$  (b),  $\text{Dy}$  (c), and  $\text{Tb}$  (d) measured at 2 K under a magnetic field of 6 T. (e) calculated XAS and XMCD spectra for non-collinear AFM order, and (f) calculated XMCD spectrum for collinear AFM order. The XMCD spectra are scaled by a factor of 10 for a clearer view.

Table 6: Spin ( $m_s$ ) and orbital ( $m_l$ ) moments measured by XMCD.

Sample	Ion	$m_s(\mu_B/\text{ion})$	$m_l(\mu_B/\text{ion})$	$m_{tot}(\mu_B/\text{ion})$	T(K)	B(T)
HoFeWO <sub>6</sub>	Fe3+	0.25	0.01	0.27	2	6
	Fe3+	0.24	0.03	0.27	12	6
	Fe3+	0.24	0.02	0.27	25	6
	Ho3+	1.56	2.54	4.1	2	6
	Ho3+	1.39	2.53	3.92	12	6
	Ho3+	1.43	2.53	3.97	25	6
DyFeWO <sub>6</sub>	Fe3+	0.49	0.03	0.52	2	6
	Fe3+	0.46	0.04	0.49	30	6
	Dy3+	1.82	1.95	3.77	2	6
	Dy3+	1.22	1.33	2.56	30	6
TbFeWO <sub>6</sub>	Fe3+	0.45	0.03	0.48	2	6
	Fe3+	0.42	0.02	0.45	30	6
	Tb3+	2.63	1.45	4.1	2	6
	Tb3+	1.84	1.1	2.93	30	6

In order to extract more detailed information about the ground state, the well-established configuration-interaction cluster calculations using the XTLS code [75] was performed to extract more detailed information about the ground state and the details are explained in [74]. The calculated XAS, as presented in Fig. 17(e) (green solid curve), is in good agreement with the experimental XAS.

On the other hand, the calculated XMCD for a collinear antiferromagnetic order, as presented in Fig. 17(f) (magenta solid curve), does not reproduce the experimental XMCD at the  $L_2$  edge. In order to improve the simulation of the XMCD a non-collinear AFM model with spins arranged 90 degrees with respect to each other, as proposed by Ghara *et al.* [28] using neutron diffraction, was considered. As presented in Fig. 17(e) (red solid curve), the non-collinear configuration of Fe spins reproduces the experimental data. The calculations show that the  $\text{Fe}^{3+}$  ions are in a high spin  $S = 5/2$  state and the magnetic moment of the single  $\text{Fe}^{3+}$  ion is  $4.6 \mu_B$ . The calculations also estimate a net moment of about  $0.26 \mu_B$  for the  $\text{Fe}^{3+}$  ions arranged in the non-collinear AFM

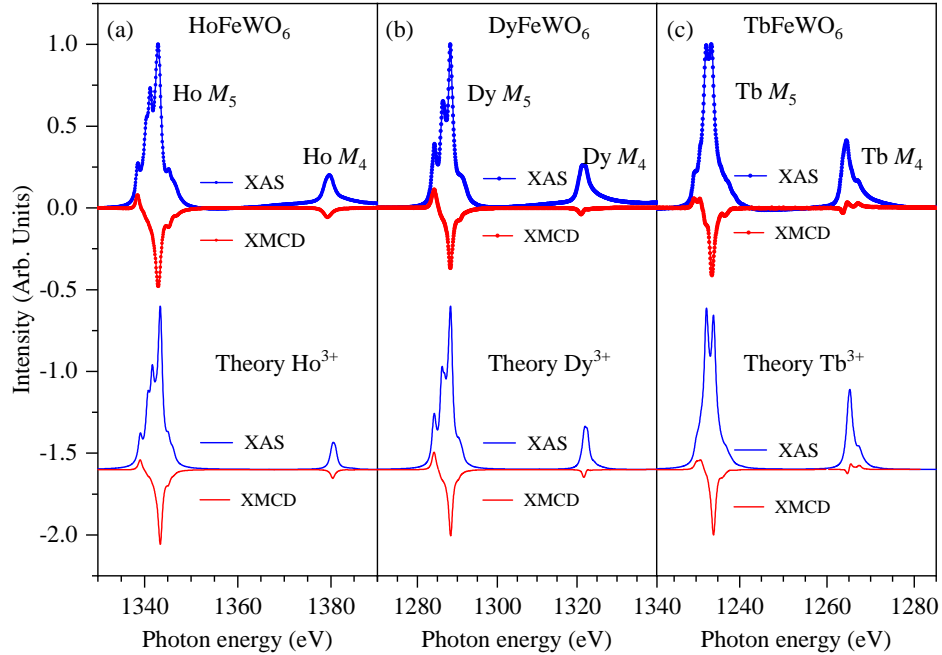


Figure 18: R  $M_{4,5}$  XAS (blue dots) and XMCD (red dots) spectra of  $R\text{FeWO}_6$  measured at 2 K under a magnetic field of 6 T, together with the calculated XAS (solid blue line) and XMCD (solid red line) of  $R^{3+}$  for R = Ho (a), Dy (b), and Tb (c).

order in presence of an applied field of 6 T, which is in very good agreement with the results of the sum rules.

Figures 18(a-c) show the R  $M_{4,5}$  XAS and XMCD measurements for R = Ho, Dy, and Tb samples, respectively, under a magnetic field of 6 T and at temperature 2 K. The moments obtained by the application of the sum rules are shown in Table 6. The simulations are consistent and have a good agreement with the experimental spectra, which demonstrates that the valence state of the R ions in  $R\text{FeWO}_6$  (R = Ho, Dy, and Tb) is  $3+$ . Contrary to the Fe  $L_{2,3}$  XMCD, the Ho  $M_{4,5}$  XMCD cannot distinguish between the collinear and non-collinear AFM order.

### 4.3 Density Functional Theory (DFT) Calculations on HoFeWO<sub>6</sub>

The orthorhombic bulk unit cell for Density Functional Theory (DFT) calculations was provided using Rietveld model on XRD measurements at 300 K. All periodic, spin-polarized DFT calculations were carried out using the Vienna *ab initio* simulation package (VASP) [59–61] version 5.4.1 and the atomic simulation environment (ASE) [62]. The details of the calculations are presented in [74]. As previously mentioned in section 4.1, the structural relaxation calculation revealed no structural transition, indicating the stability of *Pna2<sub>1</sub>* structure. The lattice parameters from the structural relaxation calculation was compared with the measurements in Table 5.

The density of states calculations also confirm that orthorhombic HoFeWO<sub>6</sub> is an insulator with a wide bandgap of 3.7 eV. Figure 19 shows the results of total density of states calculations.

The spin-polarized DFT calculations were used to estimate the oxidation states by approximating the magnetic moment of each atom without including the effects of spin-orbit coupling, and the results are presented in Table 7. By comparing this results with the electronic configuration of elemental Ho, Fe, and W, respectively as Ho: [Xe] 4*f*<sup>11</sup> 6*s*<sup>2</sup>, Fe: [Ar] 3*d*<sup>6</sup> 4*s*<sup>2</sup>, and W: [Xe] 4*f*<sup>14</sup> 5*d*<sup>4</sup> 6*s*<sup>2</sup>, and using Hund’s law we can estimate the oxidation states as 3+, 3+, and 6+, respectively. This is quite consistent with our XAS and XMCD results and also in good agreement with previous reports [28,30]. Figure 20 shows a schematics of elemental and ionic Ho, Fe, and W atoms.

### 4.4 Magnetic Properties of HoFeWO<sub>6</sub>

Figure 21 shows the temperature-dependent DC (molar) magnetic susceptibility ( $\chi(T) = M/H$ ) and the inverse susceptibility ( $\chi(T)^{-1}$ ). Figure 22(a) presents a magnified view of  $\chi(T)$  and Fig. 22(b) shows the heat capacity ( $C_p(T)$ ) data at low temperature below 25 K. The kink in  $\chi(T)$  and the lambda-shaped peak in the  $C_p(T)$  at  $T_N(T) = 17.8$  K both indicate a second-order phase transition.

Table 7: Spin magnetic moments on the atoms in units of electron spin obtained by DFT calculations.

Ion	<i>s</i>	<i>p</i>	<i>d</i>	<i>f</i>	Total
Ho1	0.001	-0.008	0.015	3.95	3.958
Ho2	0.002	0.012	-0.003	-3.94	-3.929
Ho3	0.002	0.012	-0.003	-3.94	-3.929
Ho4	0.001	-0.008	0.015	3.95	3.958
Fe1	0.011	0.024	4.172	0	4.206
Fe2	0.01	0.024	4.169	0	4.203
Fe3	0.01	0.024	4.169	0	4.203
Fe4	0.011	0.024	4.172	0	4.206
W1	0.007	0.012	0.049	0	0.067
W2	0.007	0.012	0.048	0	0.067
W3	0.007	0.012	0.048	0	0.067
W4	0.007	0.012	0.049	0	0.067
O1	0.005	0.071	0	0	0.075
O2	0.005	0.07	0	0	0.075
O3	0.005	0.07	0	0	0.075
O4	0.005	0.07	0	0	0.075
O5	0.009	0.141	0	0	0.15
O6	0.008	0.14	0	0	0.148
O7	0.008	0.14	0	0	0.148
O8	0.009	0.141	0	0	0.15
O9	0.006	0.053	0	0	0.059
O10	0.006	0.055	0	0	0.061
O11	0.006	0.055	0	0	0.061
O12	0.006	0.053	0	0	0.059
O13	0.009	0.105	0	0	0.114
O14	0.009	0.103	0	0	0.112
O15	0.009	0.103	0	0	0.112
O16	0.009	0.105	0	0	0.114
O17	0.008	0.084	0	0	0.092
O18	0.008	0.082	0	0	0.09
O19	0.008	0.082	0	0	0.09
O20	0.008	0.084	0	0	0.092
O21	0.008	0.089	0	0	0.097
O22	0.008	0.09	0	0	0.099
O23	0.008	0.09	0	0	0.099
O24	0.008	0.089	0	0	0.097

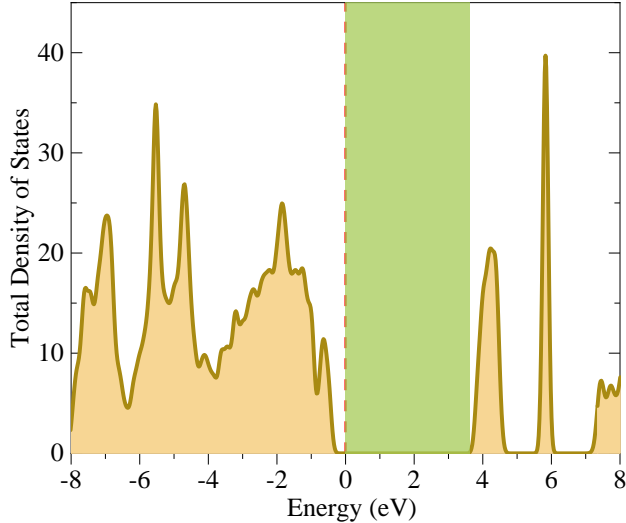


Figure 19: Total density of states for  $\text{HoFeWO}_6$ . Dashed line: Fermi energy. Highlighted region: insulating gap of  $\sim 3.7$  eV.

According to our XMCD results and also the neutron diffraction data on  $\text{DyFeWO}_6$  reported in [28], this phase transition can be interpreted as the onset of the long-range antiferromagnetic (AFM) ordering of  $S = 5/2$   $\text{Fe}^{3+}$  cations with a half-filled  $d$  shell. By lowering the temperature, as can be seen in Fig. 22(b), susceptibility shows a broad maximum at  $T_{\text{max}} = 10.8$  K and below this temperature it continues to decrease. This broad maximum is reminiscent of a low-dimensional magnetic system [76]. This behavior could be related to the way the  $\text{Ho}^{3+}$  ions are arranged inside the crystal structure. As shown previously in Fig. 15, the  $\text{Ho}^{3+}$  ions are occupying channels in between the  $\text{FeO}_6$  and  $\text{WO}_6$  octahedra, creating a quasi-one dimensional chain along the  $c$  direction.

The inverse magnetic susceptibility  $\chi^{-1}(T)$ , as shown in Fig. 21, follows the Curie-Weiss (CW) law (Eq. 54)

$$\chi^{-1}(T) = 3k_B \frac{(T - \theta_{\text{CW}})}{N_A \mu_{\text{eff}}^2} \quad (54)$$

in the paramagnetic region. Based on the CW fit, the effective total magnetic moment was estimated

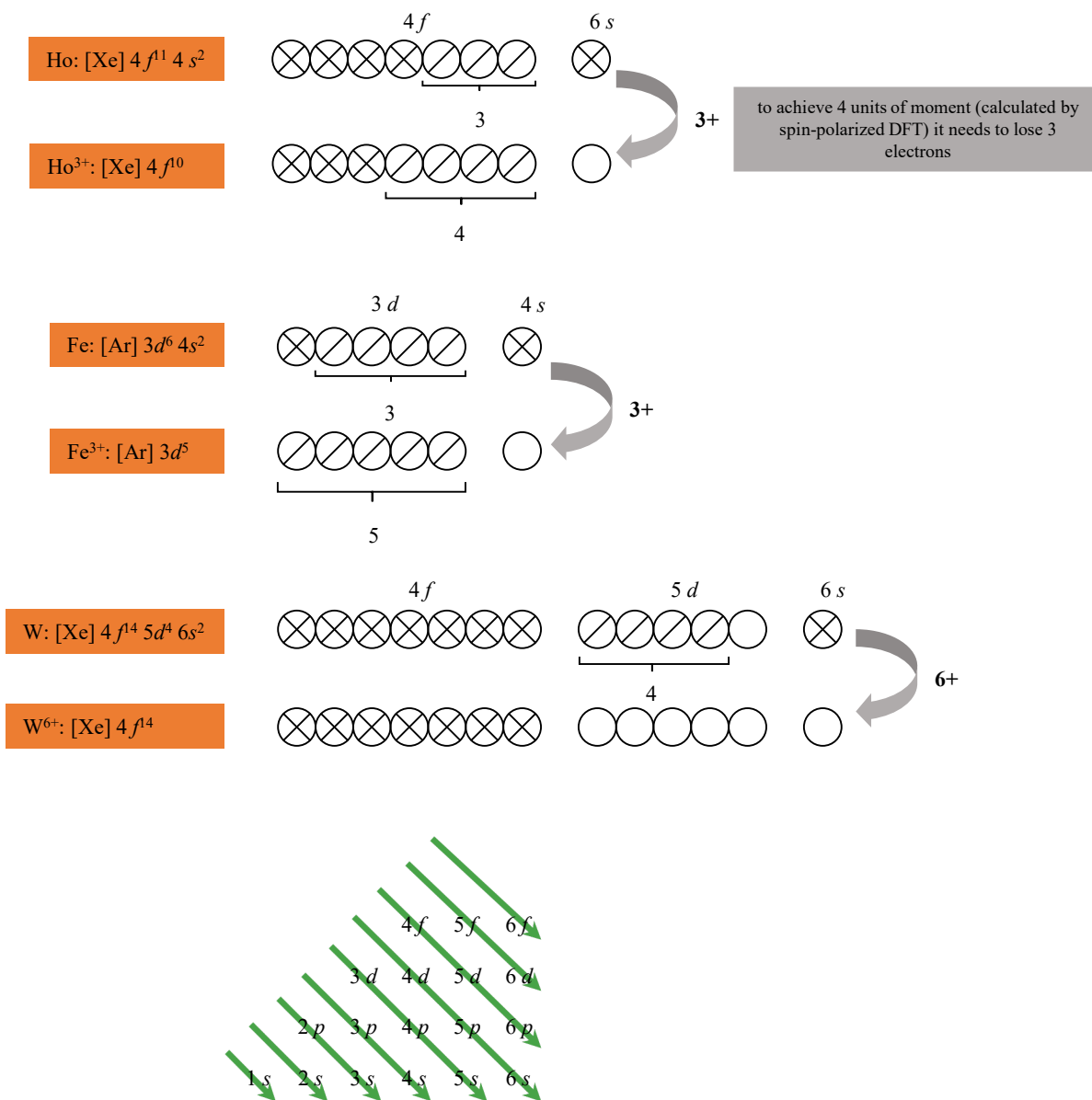


Figure 20: Schematics of elemental and ionic Ho, Fe, and W atoms. By comparing the results of magnetic moments from the spin-polarized DFT calculation with the electronic configuration of elemental Ho, Fe, and W and using Hund's law we can estimate the oxidation states as 3+, 3+, and 6+, respectively.

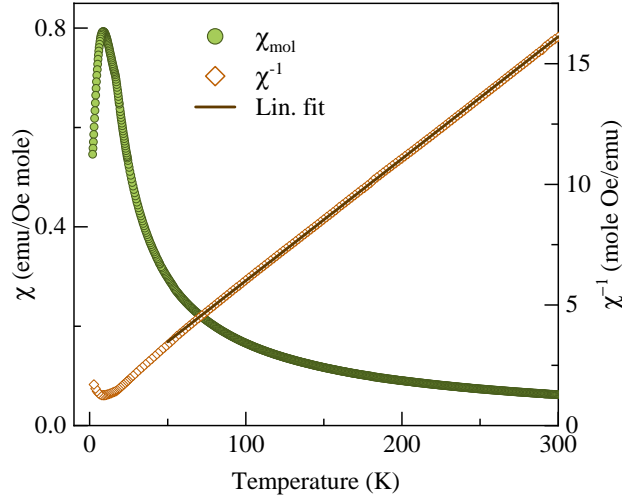


Figure 21: Temperature-dependent magnetic susceptibility,  $\chi(T)$ , of  $\text{HoFeWO}_6$  under the field-cooled condition with  $H=1$  T, its inverse,  $\chi^{-1}(T)$ , and the fit to the inverse.  $\chi^{-1}(T)$  follows the Curie-Weiss law in the paramagnetic region above  $T_N = 17.8$  K. From the fit, we find the Curie-Weiss temperature of  $\theta_{CW} = -18.88$  K and the effective magnetic moment of  $\mu_{\text{eff}} = 12.58 \mu_B/\text{f.u.}$

as  $\mu_{\text{eff}} = 12.58 \mu_B/\text{f.u.}$  which is in good agreement with the theoretical value of  $\mu_{\text{th}} = 12.14 \mu_B/\text{f.u.}$  for the  $\text{Fe}^{3+}$  and  $\text{Ho}^{3+}$  moments and the CW temperature of  $\theta_{CW} = -18.88$  K is relatively close to  $T_N = 17.8$  K. The negative sign also indicates that the dominant interaction below  $T_N$  is antiferromagnetic.

Figure 23 shows the effect of external magnetic field on  $\chi(T)$  at low temperatures. By increasing the field, the kink at 17.8 K and the broad maximum at 10.8 K slightly moves toward lower temperatures. At 100 Oe and below  $\sim 4$  K an anomaly appears which could be related to ordering of  $\text{Ho}^{3+}$  spins. This anomaly disappears as the field is increased. Increasing the field to  $\sim 2.1$  kOe also causes an uptick in the  $\chi(T)$  below  $T_N$ . At 27 kOe a small broad anomaly appears at low temperature. This could indicate a possible change in the magnetic structure of the compound under magnetic field.

We measured the AC susceptibility ( $\chi_{\text{AC}}(T)$ ) of  $\text{HoFeWO}_6$  under different external magnetic field and the results are summarized in Fig. 24. In this measurement the real part of  $\chi_{\text{AC}}(T)$  is

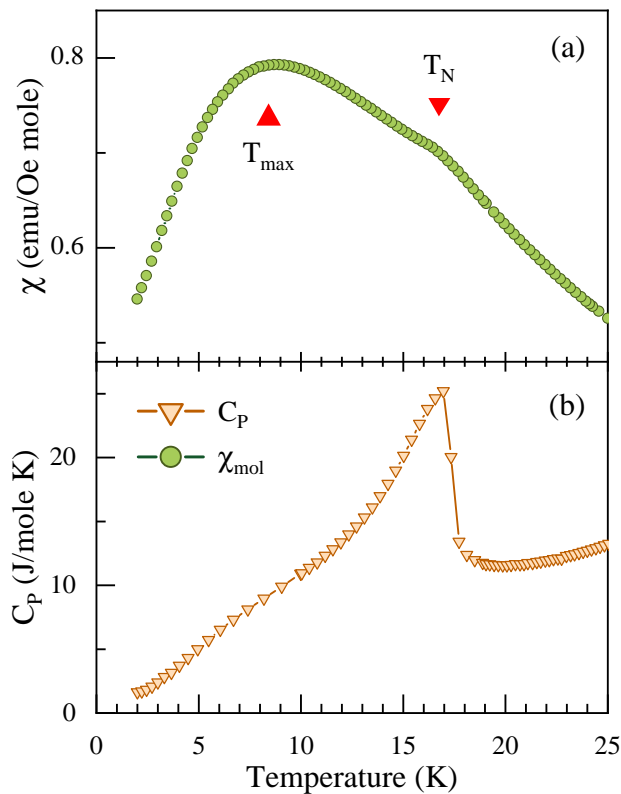


Figure 22: (a) Heat capacity and (b) magnified view of (molar) magnetic susceptibility of  $\text{HoFeWO}_6$ . Heat capacity was measured during warming without the presence of a magnetic field and magnetic susceptibility was measured under the field-cooled condition and in the presence of  $H = 1 \text{ T}$ .

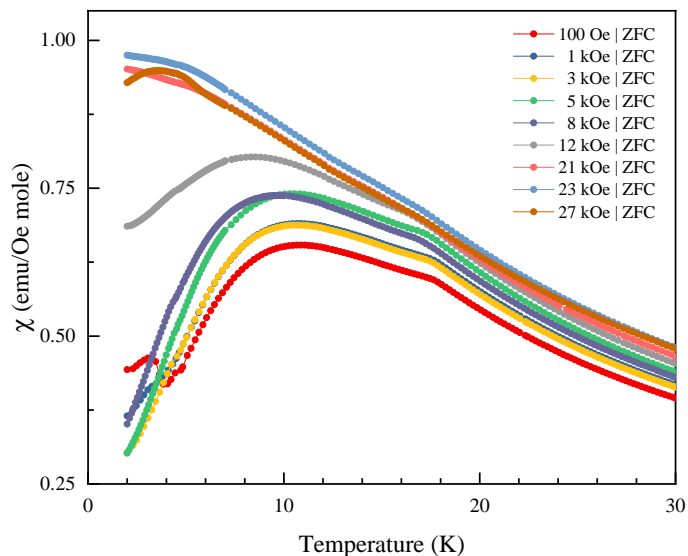


Figure 23: DC magnetic susceptibility,  $\chi(T)$ , of  $\text{HoFeWO}_6$  measured under different external magnetic fields and zero-field cooled condition.

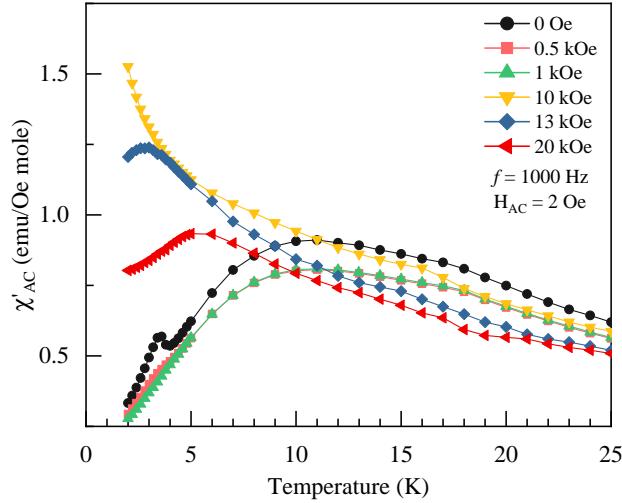


Figure 24: Real part of AC magnetic susceptibility,  $\chi_{AC}(T)$ , of  $\text{HoFeWO}_6$  measured under the frequency of  $f = 1$  kHz and a time-varying magnetic field of  $H_{AC} = 2$  Oe and under different external magnetic fields.

measured as a response of the sample to a small time-varying magnetic field of  $H_{AC} = 2$  Oe with the frequency  $f = 1$ . The curve at 0 Oe is, in essence, similar to DC susceptibility. The broad peak at  $T_{\max} = 10.8$  K, as mentioned before, is characteristic of low-dimensional magnets and is likely due to formation of a regime of short-range correlation between  $\text{Ho}^{3+}$  [76]. A small peak appears at  $\sim 3.5$  K, which indicates the ordering of  $\text{Ho}^{3+}$  spins. It was shown for  $\text{DyFeWO}_6$  by neutron diffraction measurements that the ordering of  $\text{Fe}^{3+}$  spins induces the ordering of  $\text{Dy}^{3+}$  through a cooperative process at  $T_N$ . The peak at 3.5 K can be suppressed with a magnetic field of 1 kOe. The AC susceptibility adopts the uptick behavior below  $T_N$  at a relatively lower field of  $\sim 10$  kOe comparing to 27 kOe in case of DC susceptibility.  $\chi_{AC}(T)$  was also measured at two other frequencies ( $f = 10$  Hz and 100 Hz) without external magnetic field. The results are shown in Fig. 25 and show a largely overlapping data within the resolution of our measurement, which indicates a lack of glassy behavior.

Figure 26(a) and (b) shows the field-dependent DC magnetization ( $M(H)$ ) and its derivative

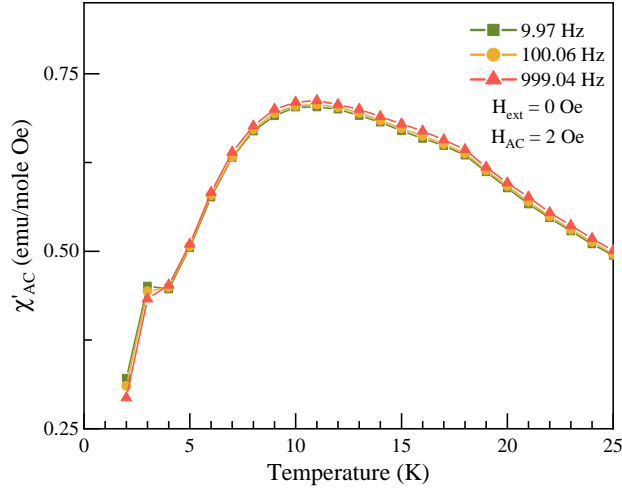


Figure 25: Real part of AC magnetic susceptibility of  $\text{HoFeWO}_6$  as function of temperature,  $\chi_{AC}(T)$ , measured under different frequencies of  $f = 10, 100,$  and  $1000$  Hz. The time-varying magnetic field is  $H_{AC} = 2$  Oe and the external magnetic field is zero.

(dM/dH) at various temperatures, respectively. The data below  $T_N$  is consistent with the AFM nature of the sample. The maximum moment that the sample gains at the lowest temperature (2 K) and the highest measured field (50 kOe) is  $\sim 4.9 \mu_{\text{eff}}/\text{f.u.}$ , which is lower than the theoretical value of  $12.4 \mu_{\text{eff}}/\text{f.u.}$ , indicating that the magnetic moments are not saturated. Graphs below 5 K show a metamagnetic behavior which indicates a competing interaction between the two sublattices ( $\text{Fe}^{3+}$  and  $\text{Ho}^{3+}$ ) in the compound. This is more evident from dM/dH, where the two peak at 2 K could be due to a spin-flop transition and seem to weaken and merge as the temperature is increased.

In figure 27 isothermal AC magnetization is presented. Since  $\chi_{AC}$  is the response of the sample to a small time-varying magnetic field, the  $\chi_{AC}(H)$  is reminiscent of dM/dH. This figure show that the two peak at 2 K continuously weakens and diminishes. The emergence of this spin-flop transition coincides with the ordering temperature of  $\text{Ho}^{3+}$  spins, which suggests that  $\text{Ho}^{3+}$   $4f$  spins and their interaction with the  $\text{Fe}^{3+}$   $3d$  spins plays an important role in the observed metamagnetic behavior.

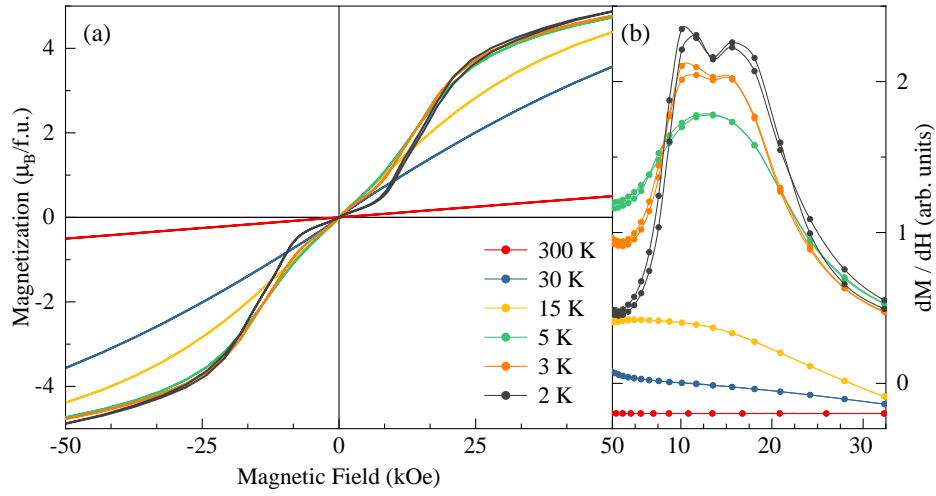


Figure 26: (a) Field-dependent DC magnetization,  $M(H)$ , at different temperatures and (b) its derivative. For clarity, the derivatives are shifted in the vertical direction.

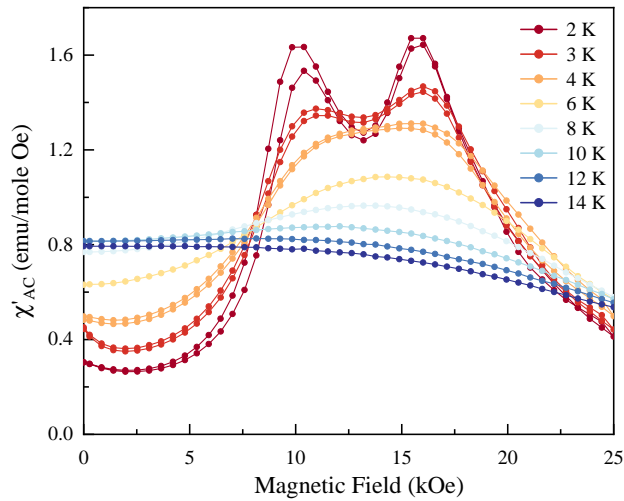


Figure 27: Real part of AC magnetic susceptibility as a function of magnetic field,  $\chi_{ac}(H)$ , measured at different temperatures.

## 4.5 Magnetic Properties of DyFeWO<sub>6</sub> and TbFeWO<sub>6</sub>

Figures 28 and 29 show  $\chi(T)$  for DyFeWO<sub>6</sub> and TbFeWO<sub>6</sub>, respectively. The kink at  $T = 18$  K in Fig. 28, represents the AFM ordering of Fe<sup>3+</sup> and the step at  $\sim 4.5$  K indicates the ordering of Dy<sup>3+</sup> in DyFeWO<sub>6</sub> sample. The magnetic response of DyFeWO<sub>6</sub> below  $T_N$  shows a broad maximum, similar to HoFeWO<sub>6</sub>, at  $T_{\max} = 12.5$ . The  $\chi(T)$  of TbFeWO<sub>6</sub>, however, shows only a peak at  $T = 2.4$  K without an anomaly around ordering of Fe<sup>3+</sup>. The heat capacity data by Ghara *et. al* [28] suggests the long-range ordering of Fe<sup>3+</sup> and Tb<sup>3+</sup> to occur in this sample at 15 K and 2.4 K, respectively.

Figure 30(a) shows the isothermal magnetization curves ( $M(H)$ ) for Dy sample and Fig. 30(b) shows its derivative,  $dM/dH$ . The curves below the  $T_N = 18$  K are consistent with the AFM nature of the compound. At low temperature, similar to Ho sample, we observe a metamagnetic behavior, indicating the possible formation of correlation between Dy<sup>3+</sup> and Fe<sup>3+</sup> spins. Figure 31(a) and (b) also show the  $M(H)$  and  $dM/dH$  curves, respectively, for Tb sample. The data shows a metamagnetic behavior of Tb<sup>3+</sup> at low temperature as well.

## 4.6 Ferroelectricity, Magnetocapacitance Effect and Magnetoelectric Coupling in HoFeWO<sub>6</sub>

Figure 32 shows the real part of dielectric constant ( $\epsilon$ ) and the imaginary part (loss tangent  $\tan(\delta)$ ) in the inset, measured at the frequency  $f = 1$  kHz and different magnetic field. The data shows a peak at 17.8 K and 0 Oe, which signals a ferroelectric (FE) transition. Similar anomaly was observed for DyFeWO<sub>6</sub>, for which the onset temperature does not change at different frequencies [28]. This indicates that the dielectric anomaly in this series is not caused by relaxation phenomena. The FE transition is further confirmed by observation of a switchable polarization, as will be

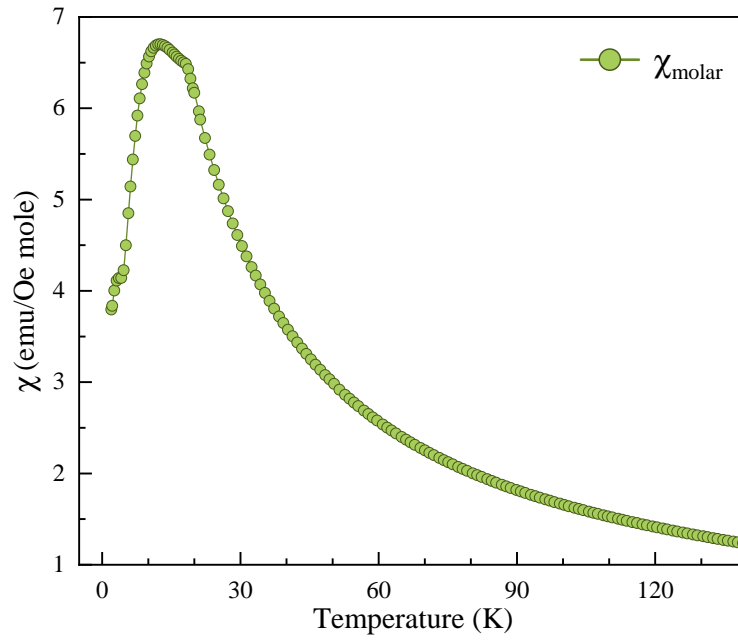


Figure 28: DC magnetic susceptibility,  $\chi(T)$ , of  $\text{DyFeWO}_6$  measured under external magnetic field of 100 Oe and zero-field cooled condition.

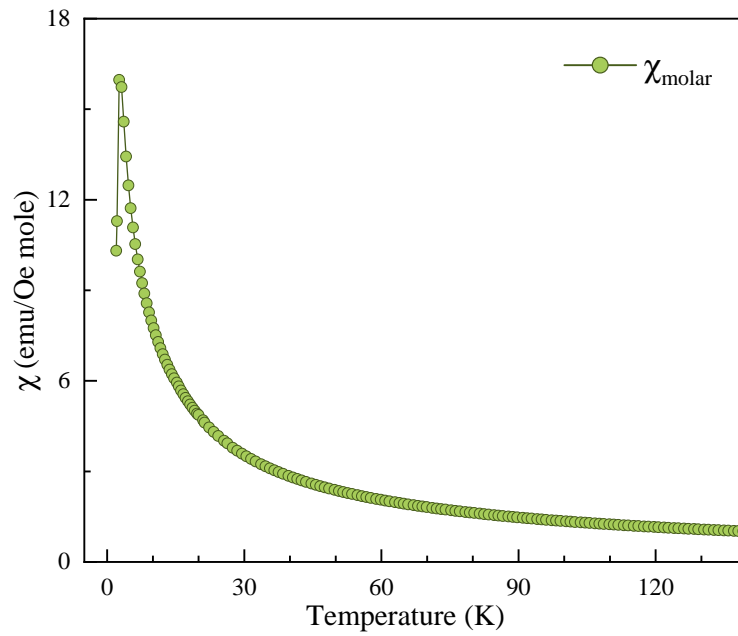


Figure 29: DC magnetic susceptibility,  $\chi(T)$ , of  $\text{TbFeWO}_6$  measured under external magnetic field of 100 Oe and zero-field cooled condition.

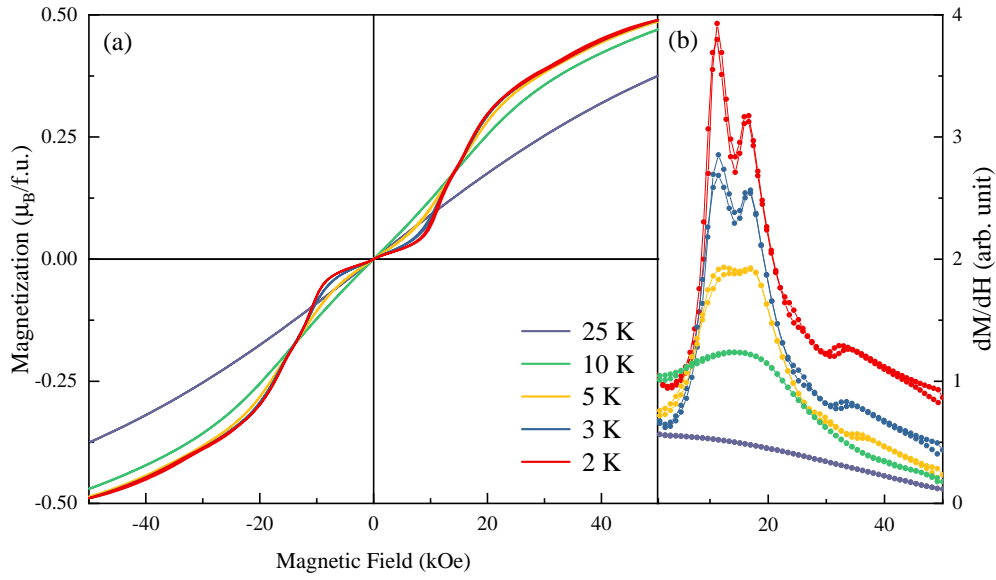


Figure 30: (a) Field-dependent DC magnetization,  $M(H)$ , of  $\text{DyFeWO}_6$  at different temperatures and (b) its derivative. For clarity, the derivatives are shifted in the vertical direction.

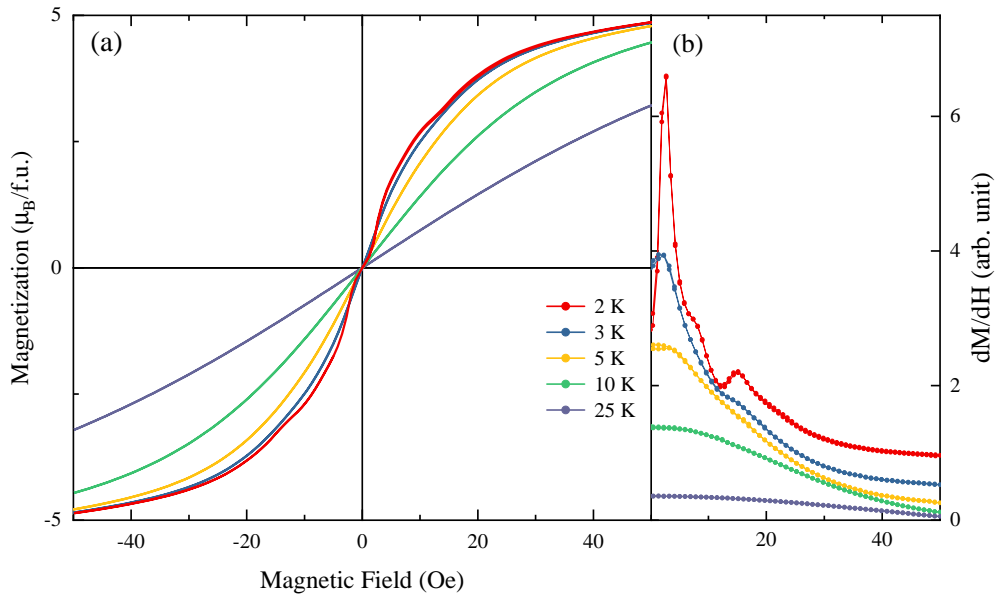


Figure 31: (a) Field-dependent DC magnetization,  $M(H)$ , of  $\text{TbFeWO}_6$  at different temperatures and (b) its derivative. For clarity, the derivatives are shifted in the vertical direction.

shown later in Fig. 34, and the peak in  $\text{Tan}(\delta)$ , as shown in the inset to Fig. 32. The fact that the FE transition temperature coincides with the  $T_N$  favors the proposition that the observed ferroelectricity originates from the spin ordering. It is also visible that the magnetic field suppresses the FE peak at 17.8 K.

The fact that similar FE transition is also observed in  $\text{YFeWO}_6$ , with non-magnetic rare-earth ion indicates that the ferroelectric transition in this series of compounds is caused by ordering of  $\text{Fe}^{3+}$  spins [28]. This also means that if dielectric anomaly in  $\text{DyFeWO}_6$  is independent of frequency and the ferroelectric transition does not have an origin in relaxation phenomena, then it should hold true for other compounds of this family with different rare-earth. Furthermore, one of the features that distinguishes relaxor behavior from true ferroelectric behavior is the specific temperature dependence of the static susceptibility with a maximum. In particular, the maximum (or peak) in the static dielectric susceptibility can be well characterized by a relationship that is essentially a Lorentz form function. The dynamic behavior of the relaxors merely qualifies the materials as different types of relaxors [77]. The dielectric peak in Fig. 32 resembles a lambda-shaped peak and not a Lorentz form.

A typical pyrocurrent ( $I_{\text{pyro}}(T)$ ) measurement at two different warming rate is shown in Fig. 33. As we can see, the peak in  $I_{\text{pyro}}(T)$  does not move by increasing the warming rate. This observation shows that the pyrocurrent is caused by depolarization of ferroelectric dipoles. The temperature-dependent electric polarization ( $\Delta P(T)$ ) is obtained by integrating the  $I_{\text{pyro}}(T)$  and Fig. 34 summarizes our results and the effect of external magnetic field on  $\Delta P(T)$ .

As mentioned, the polarization in these compounds is caused by the ordering of the  $\text{Fe}^{3+}$  spins [28] and the fact that the  $\text{Fe}^{3+}$  spins are arranged in a non-collinear fashion indicates that the inverse Dzyaloshinskii-Moriya (DM) interaction is likely the underlying mechanism in breaking

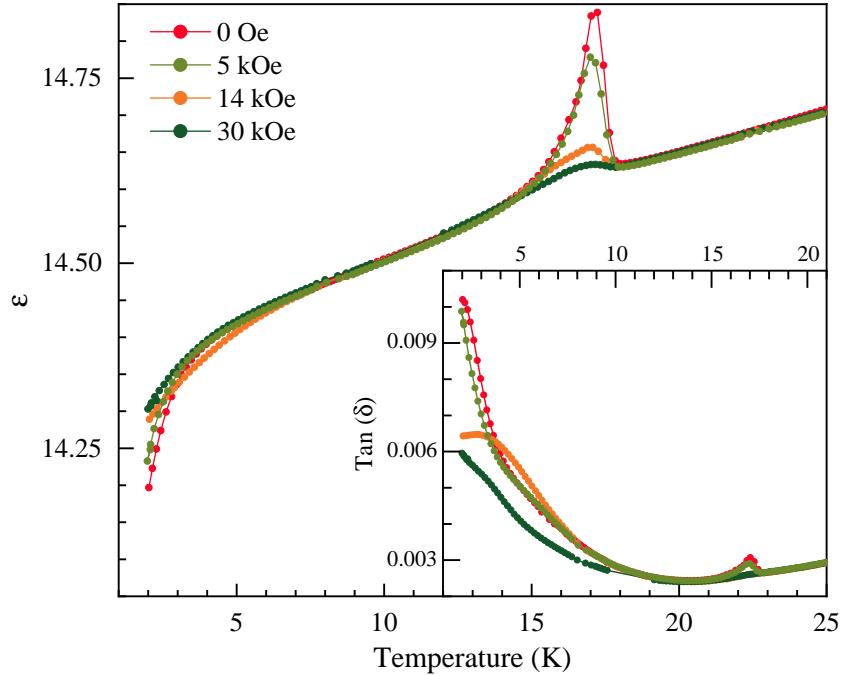


Figure 32: Temperature-dependent dielectric constant of  $\text{HoFeWO}_6$  under different magnetic fields measured under the field-cooled condition, with the loss tangent,  $\text{Tan}(\delta)$ , in the inset. The data were collected at the frequency of  $f = 1$  kHz.

the inversion symmetry by magnetic ordering [6, 45].

The effect of magnetic field on the dielectric constant and its strong influence on  $\Delta P(T)$ , indicates the presence of strong magnetoelectric (ME) coupling in this system. The polarization at  $H = 0$  Oe reaches a maximum at  $\sim 8.5$  K below which it slightly decreases. This behavior is in contrast to the polarization observed for  $\text{YFeWO}_6$  with a non-magnetic rare-earth cations, in which polarization saturates below  $T_N$ . The fact that the decrease in  $\Delta P(T)$  occurs below  $T_{\text{max}}$ , the temperature region in which short-range correlations between  $\text{Ho}^{3+}$  is formed, implies that the development of the  $\text{Ho}^{3+}$  magnetic sublattice and its interaction with  $\text{Fe}^{3+}$  is likely the cause for the decrease in the polarization.

We used field-dependent capacitance ( $\epsilon(H)$ ) to further study the ME coupling in this system. Magneto-capacitance (MC) effect can be used as an indirect way to measure ME coupling [11].

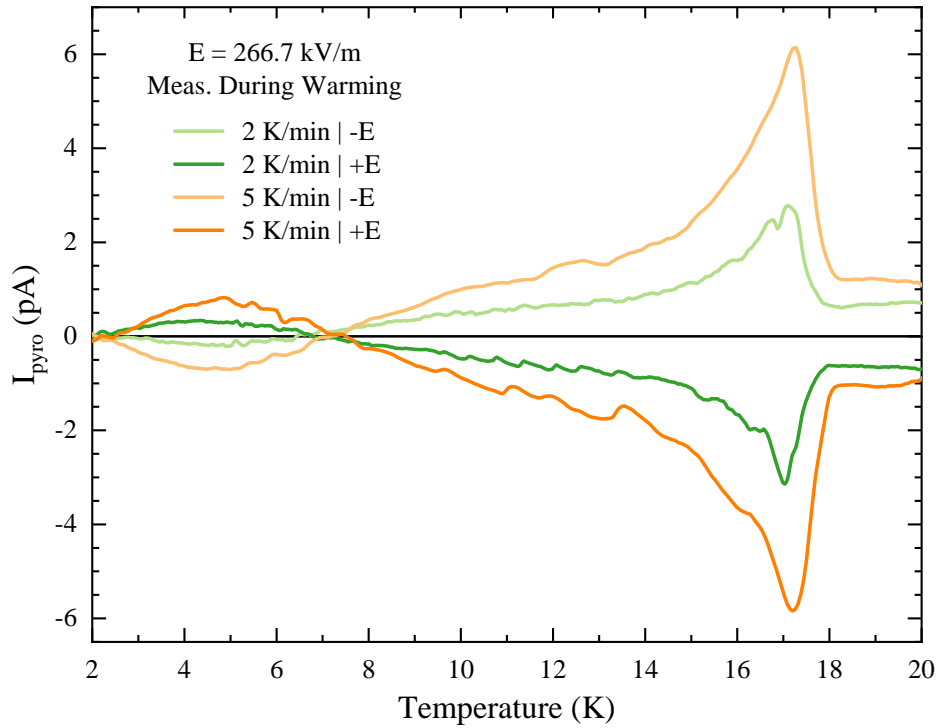


Figure 33: Examples of pyrocurrent as a function of temperature,  $I_{\text{pyro}}(T)$ , measured for  $\text{HoFeWO}_6$  under zero magnetic field. To measure  $I_{\text{pyro}}(T)$ , the sample was cooled down from 20 K to the base temperature of 2 K in the presence of the poling field  $E$ . The magnitude of  $E$  is the same but poling fields of opposite signs both were used. The released pyrocurrent was measured under different warming rates after the poling field was turned off. The fact that the peaks in  $I_{\text{pyro}}(T)$  under different warming rate occur in the same temperature indicates that the released pyrocurrent is due to ferroelectric polarization.

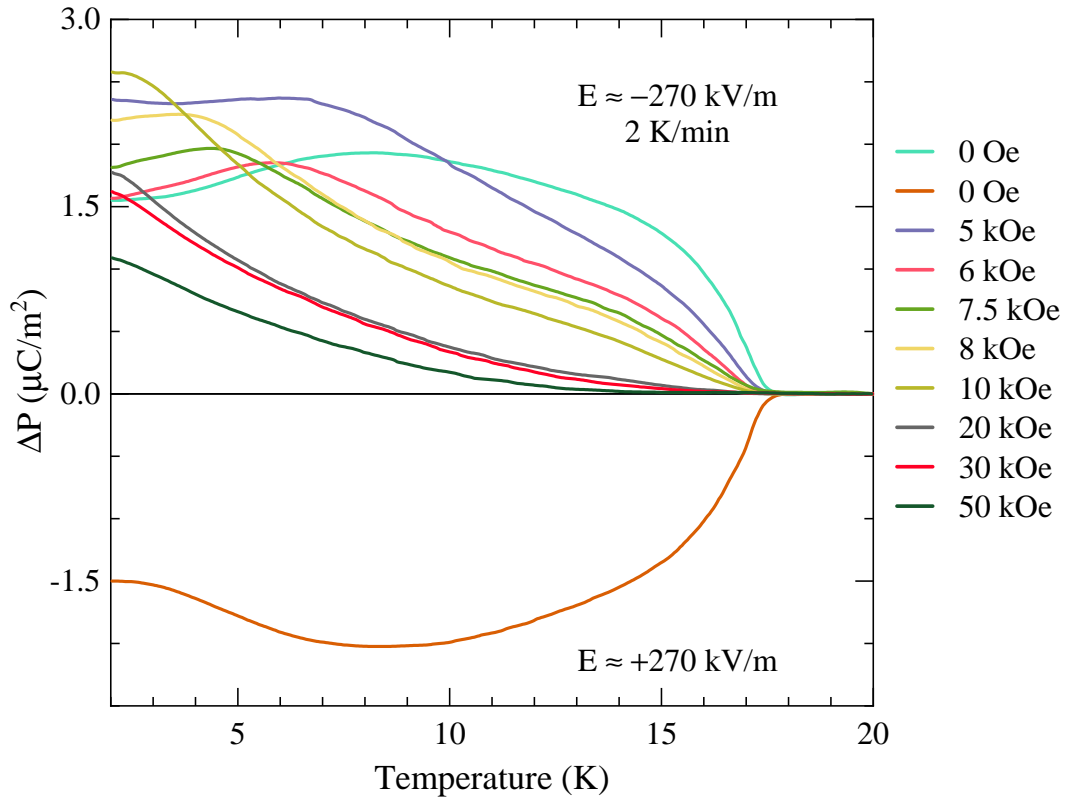


Figure 34: Electric polarization as a function of temperature,  $\Delta P(T)$ , for  $\text{HoFeWO}_6$  under different magnetic fields.  $\Delta P(T)$  is obtained by integrating the  $I_{\text{pyro}}(T)$  as a function of time. The  $I_{\text{pyro}}(T)$  is measured after sample is poled with an electric field  $E = 270 \text{ kV/m}$  and during the warming at the rate of  $2 \text{ K/min}$  and under different magnetic fields.

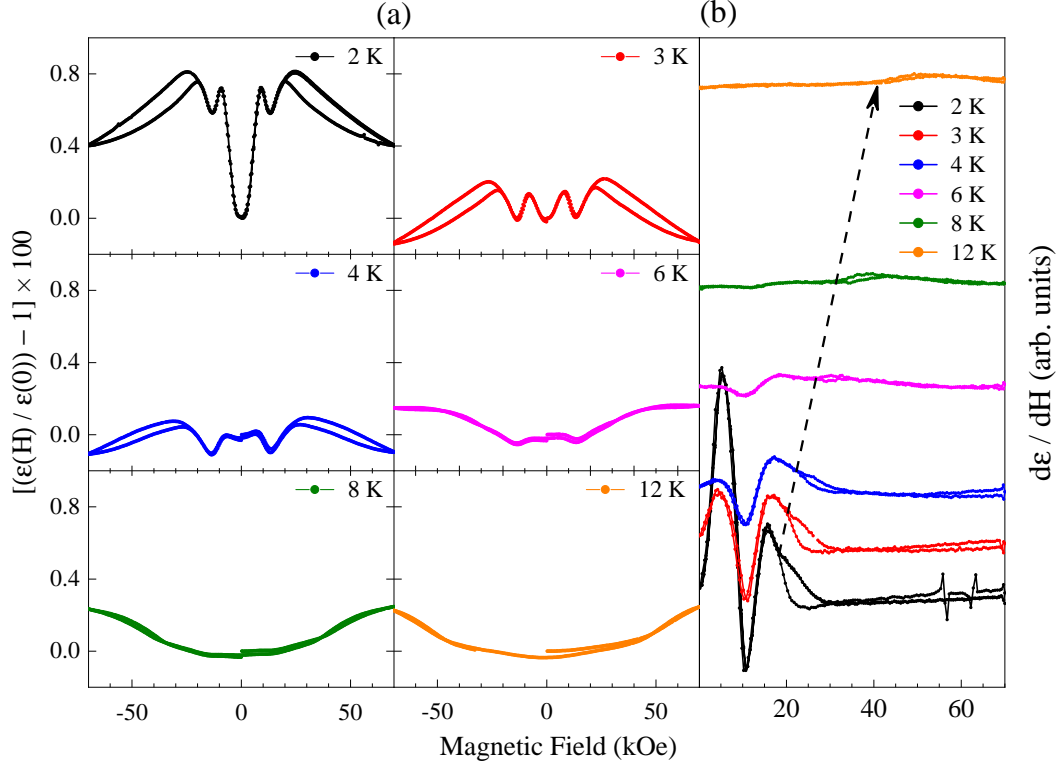


Figure 35: (a) Field-dependent dielectric constant,  $\epsilon(H)$ , of  $\text{HoFeWO}_6$  at different temperatures, normalized by the expression  $[(\epsilon(H)/\epsilon(0)) - 1] \times 100$ , (b) Derivative of  $\epsilon(H)$  at different temperatures with respect to the field. The curves are shifted vertically by distances equal to their temperature differences for clarity. The arrow shows the linear shift in the hysteresis toward higher fields as the temperature is increased.

Figure 35(a) shows the isothermal dielectric constant, which shows an MC effect with a double-hysteresis behavior. The data has been normalized with the formula  $[(\epsilon(H)/\epsilon(0)) - 1] \times 100$ . The results show a direct correspondence with the magnetization data in Fig. 26. The derivative of MC with respect to the magnetic field is shown in Fig. 35(b) and it shows a clear hysteresis region below 6 K, which seems to persist to higher temperature. Graphs in Fig. 35(b) are shifted in  $y$  direction, for clarity, by distances equal to their temperature differences. It is clear from this figure that the hysteresis region moves toward higher fields in a linear fashion as the temperature is increased.

We used the temperature-dependent  $\Delta P(T)$  at different fields to construct a  $\Delta P(H)$  graph and

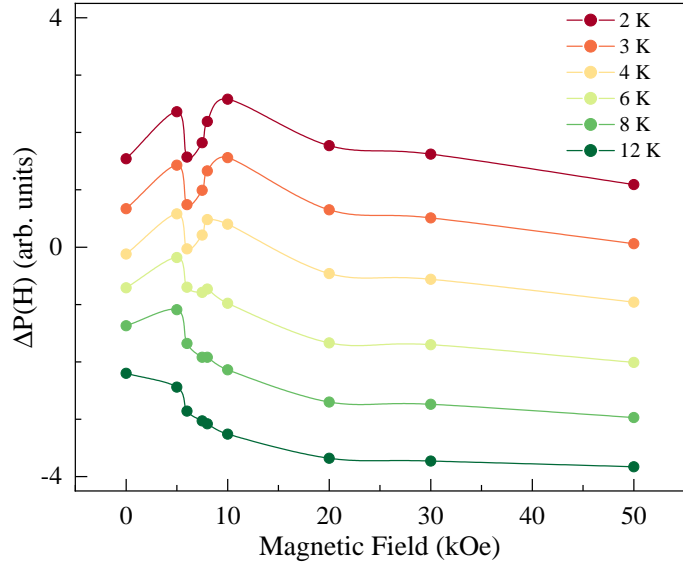


Figure 36: Electric polarization as a function of field,  $\Delta P(H)$ , at different temperatures.

the result is shown in Fig. 36. This result, interestingly enough, shows a direct correspondence with the magnetization data in Fig. 26. As we can see the data below  $\sim 6$  K is echoed by the the MC and magnetization results. This observation indicates that the mutual interplay between  $\text{Ho}^{3+} 4f$  and  $\text{Fe}^{3+} 3d$  spins is likely plays an important role in the change in the polarization under magnetic field below  $\sim 6$  K. The MC effect can be caused by different factors, however, the observation of the change in polarization by magnetic field and the  $\Delta P(H)$  curves supports the proposition that the MC effect in this compound is due to ME coupling.

#### 4.7 Magnetocapacitance Effect and Magnetoelectric Coupling in $\text{DyFeWO}_6$ and $\text{TbFeWO}_6$

In addition to  $\text{HoFeWO}_6$ , we have indirectly studied the ME coupling by measuring the MC effect in  $\text{DyFeWO}_6$  and  $\text{TbFeWO}_6$ . Figures 37 and 38 show the dielectric constant of Dy and Tb samples, respectively. The inset to each graph is the  $\text{Tan}(\delta)$ . Our results are consistent with the ferroelectric transition at the magnetic ordering temperature of  $\text{Fe}^{3+}$  in these compounds, as indicated in earlier

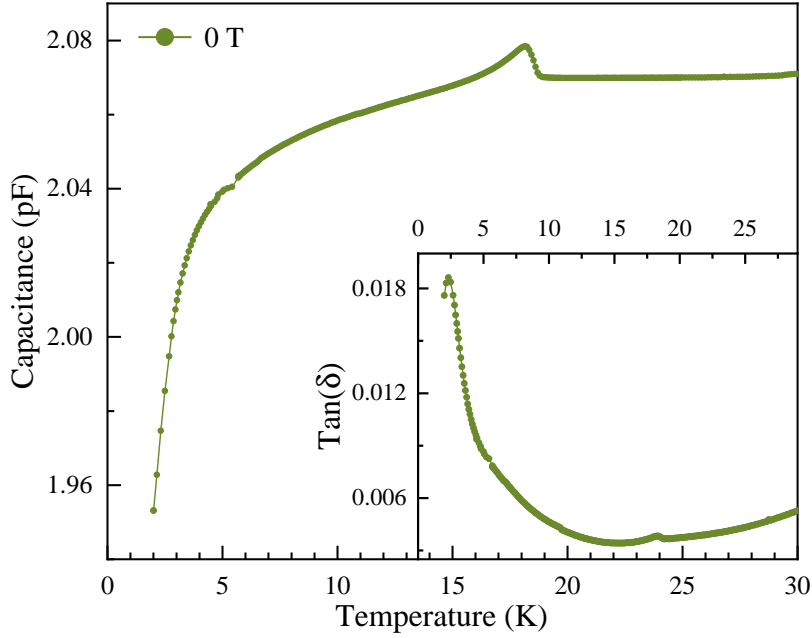


Figure 37: Capacitance of  $\text{DyFeWO}_6$  as a function of temperature measured under the field-cooled condition, with the loss tangent,  $\text{Tan}(\delta)$ , in the inset. The data were collected at the frequency of  $f = 1$  kHz.

report [28].

The field-dependent dielectric constant ( $\epsilon(H)$ ) measurements of  $\text{DyFeWO}_6$  and  $\text{TbFeWO}_6$  are presented in Fig. 39 and 40, respectively. The results, similar to  $\text{HoFeWO}_6$ , shows an MC effect. We have not measured  $\Delta P(T)$  for  $\text{DyFeWO}_6$  and  $\text{TbFeWO}_6$ , however, according to the results of  $\text{HoFeWO}_6$ , the observed MC effect is likely due to ME coupling.

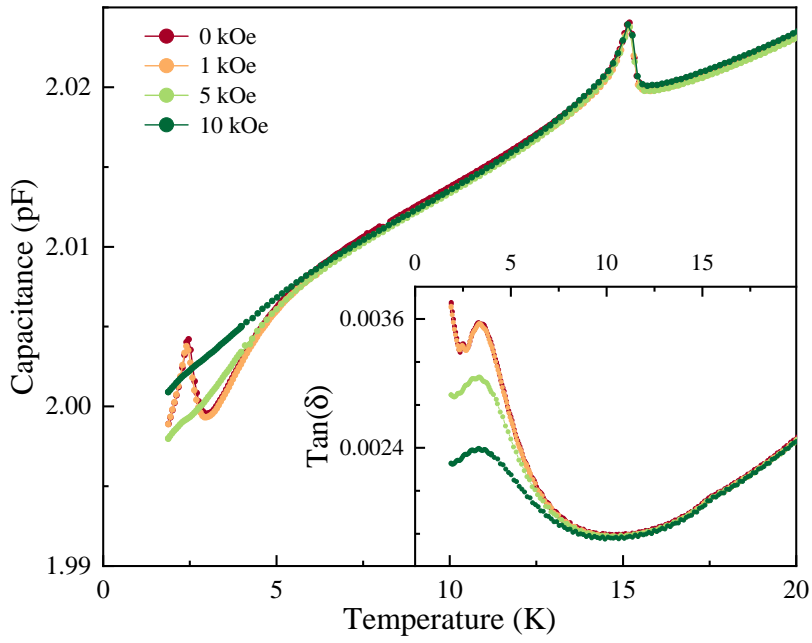


Figure 38: Capacitance of  $\text{TbFeWO}_6$  as a function of temperature measured at different magnetic fields and under the field-cooled condition, with the loss tangent,  $\text{Tan}(\delta)$ , in the inset. The data were collected at the frequency of  $f = 1$  kHz.

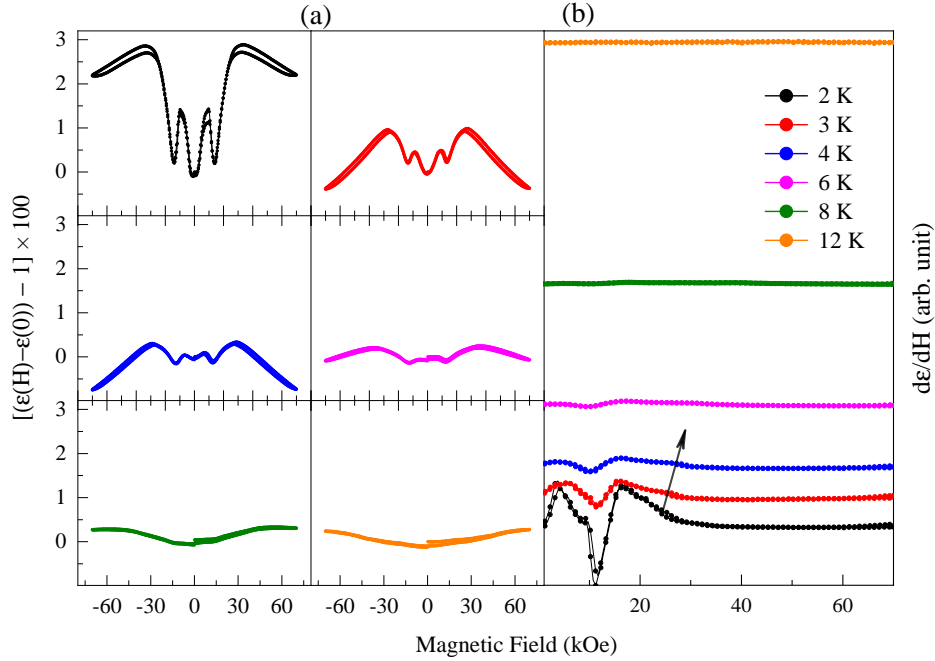


Figure 39: (a) Field-dependent dielectric constant,  $\epsilon(H)$ , of DyFeWO<sub>6</sub> at different temperatures, normalized by the expression  $[\epsilon(H)/\epsilon(0) - 1] \times 100$ , (b) Derivative of  $\epsilon(H)$  at different temperatures with respect to the field. The curves are shifted vertically by distances equal to their temperature differences for clarity. The arrow shows the linear shift in the hysteresis toward higher fields as the temperature is increased.

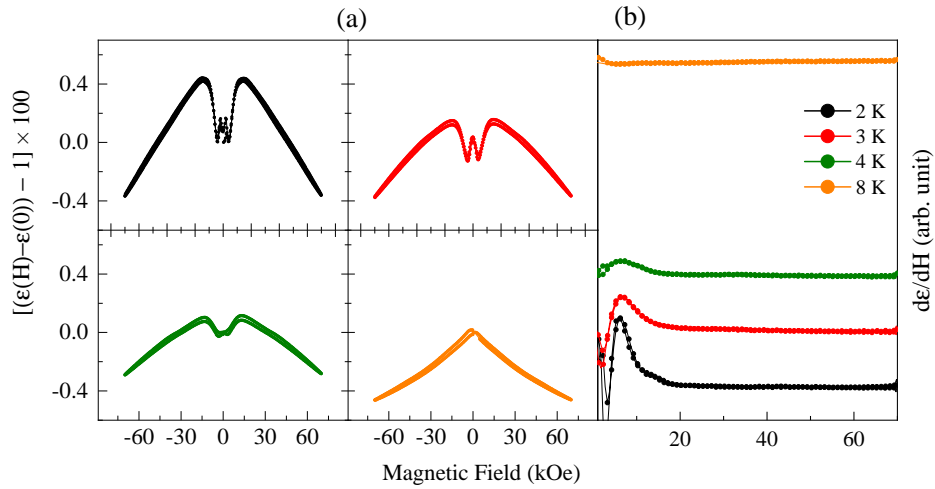


Figure 40: (a) Field-dependent dielectric constant,  $\epsilon(H)$ , of TbFeWO<sub>6</sub> at different temperatures, normalized by the expression  $[\epsilon(H)/\epsilon(0) - 1] \times 100$ , (b) Derivative of  $\epsilon(H)$  at different temperatures with respect to the field. The curves are shifted vertically by distances equal to their temperature differences for clarity. The arrow shows the linear shift in the hysteresis toward higher fields as the temperature is increased.

## 5 Summary and Conclusion

We have studied the multiferroic properties of, and magnetoelectric coupling in, the type-II multiferroics  $R\text{FeWO}_6$  ( $R = \text{Ho}, \text{Dy}, \text{and Tb}$ ).

Through XRD measurements, we found the crystal structure to belong to the polar space group  $Pna2_1$  and no structural phase transition was observed down to 8 K for  $\text{HoFeWO}_6$ . DFT calculations for  $\text{HoFeWO}_6$  also confirmed that this compound is stable in the  $Pna2_1$  structure. XAS and XMCD measurements on  $R = \text{Ho}, \text{Dy}, \text{and Tb}$  samples show an oxidation state of 3+ for the Fe and  $R$  cations. Simulation of XMCD data suggests that the  $\text{Fe}^{3+}$  spins are arranged in a non-collinear fashion at angles of 90 degrees with respect to each other.

The AFM and ferroelectric ordering at  $T_N = 17.8, 18$  and 15 K confirm the multiferroic nature of these compounds. All of these observations favor the AFM ordering of  $\text{Fe}^{3+}$  as the origin of the ferroelectric transition, with inverse DM interaction playing an important role in breaking the inversion symmetry.

Magnetic susceptibility of  $\text{HoFeWO}_6$  below  $T_N$  shows a broad maximum at  $T_{\text{max}} \sim 10.8$  K, which usually relates to a magnetic system with reduced dimensionality, and the ordering of  $\text{Ho}^{3+}$  spins at  $\sim 3.5$  K. The decrease in polarization below  $T_{\text{max}}$  also seems to be related to the low-dimensional nature of the  $\text{Ho}^{3+}$  spins and the development in their magnetic sublattice.

The responses of both the dielectric constant and the polarization to the magnetic field reveal the presence of ME coupling in all compounds. We used the MC effect to indirectly investigate the ME coupling and found that the field-dependent dielectric constant shows a direct correspondence with magnetization data. The polarization response of  $\text{HoFeWO}_6$  to the magnetic field, especially  $\Delta P(H)$  and its correspondence with the  $M(H)$  curves, further supports the presence of ME coupling in this compound. The magnetization and MC data of  $\text{HoFeWO}_6$  below  $\sim 6$  K, in particular, are

qualitatively echoed by  $\Delta P(H)$ , which implies the effect of mutual interaction between  $\text{Ho}^{3+}$   $4f$  and  $\text{Fe}^{3+}$   $3d$  spins on the ME coupling.

Considering the non-collinear arrangement of spins in these compounds, spin-orbit coupling likely plays a crucial role in the observed ME coupling, although contributions from other possible factors, *e.g.* magnetostriction, cannot be ignored. A substantiated and definite description of the mechanism for ME coupling requires further detailed single-crystal study.

## Bibliography

- [1] G. A. Smolenskiĭ and I. E. Chupis, “Ferroelectromagnets,” *Soviet Physics Uspekhi*, vol. 25, pp. 475–493, Jul 1982.
- [2] T. Kimura, T. Goto, H. Shintani, K. Ishizaka, T. Arima, and Y. Tokura, “Magnetic control of ferroelectric polarization,” *Nature*, vol. 426, pp. 55–58, Nov 2003.
- [3] H. Katsura, N. Nagaosa, and A. V. Balatsky, “Spin current and magnetoelectric effect in noncollinear magnets,” *Physical Review Letters*, vol. 95, pp. 1–4, Jul 2005.
- [4] M. Mostovoy, “Ferroelectricity in spiral magnets,” *Physical Review Letters*, vol. 96, p. 067601, Feb 2006.
- [5] N. A. Spaldin and M. Fiebig, “The renaissance of magnetoelectric multiferroics,” *Science*, vol. 309, pp. 391–392, Jul 2005.
- [6] D. Khomskii, “Classifying multiferroics: mechanisms and effects,” *Physics*, vol. 2, p. 20, Mar 2009.
- [7] B. Lorenz, Y. Q. Wang, Y. Y. Sun, and C. W. Chu, “Large magnetodielectric effects in orthorhombic HoMnO<sub>3</sub> and YMnO<sub>3</sub>,” *Physical Review B*, vol. 70, p. 212412, Dec 2004.
- [8] B. Lorenz, A. P. Litvinchuk, M. M. Gospodinov, and C. W. Chu, “Field-Induced reentrant novel phase and a ferroelectric-magnetic order coupling in HoMnO<sub>3</sub>,” *Physical Review Letters*, vol. 92, p. 087204, Feb 2004.
- [9] B. Lorenz, F. Yen, M. M. Gospodinov, and C. W. Chu, “Field-induced phases in HoMnO<sub>3</sub> at low temperatures,” *Physical Review B*, vol. 71, p. 014438, Jan 2005.
- [10] M. Fiebig, “Revival of the magnetoelectric effect,” *Journal of Physics D: Applied Physics*, vol. 38, Apr 2005.
- [11] W. Eerenstein, N. D. Mathur, and J. F. Scott, “Multiferroic and magnetoelectric materials,” *Nature*, vol. 442, pp. 759–765, Aug 2006.
- [12] R. P. Chaudhury, B. Lorenz, Y. Q. Wang, Y. Y. Sun, and C. W. Chu, “Magnetic field induced ferroelectricity in Mn<sub>0.9</sub>Fe<sub>0.1</sub>WO<sub>4</sub>,” *Journal of Applied Physics*, vol. 103, p. 07E312, Apr 2008.
- [13] N. Poudel, K.-C. Liang, Y.-Q. Wang, Y. Y. Sun, B. Lorenz, F. Ye, J. A. Fernandez-Baca, and C. W. Chu, “Magnetic-field-induced spontaneous polarization reversal in multiferroic Mn<sub>0.85</sub>Co<sub>0.15</sub>WO<sub>4</sub>,” *Physical Review B*, vol. 89, p. 054414, Feb 2014.
- [14] B. Lorenz, “Hexagonal Manganites—(RMnO<sub>3</sub>): Class (I) Multiferroics with Strong Coupling of Magnetism and Ferroelectricity,” *ISRN Condensed Matter Physics*, vol. 2013, pp. 1–43, Nov 2013.
- [15] B. B. Van Aken, T. T. Palstra, A. Filippetti, and N. A. Spaldin, “The origin of ferroelectricity in magnetoelectric YMnO<sub>3</sub>,” *Nature Materials*, Feb 2004.

- [16] M. Lilienblum, T. Lottermoser, S. Manz, S. M. Selbach, A. Cano, and M. Fiebig, “Ferroelectricity in the multiferroic hexagonal manganites,” *Nature Physics*, vol. 11, pp. 1070–1073, Dec 2015.
- [17] N. A. Spaldin, “Multiferroics beyond electric-field control of magnetism,” *Proceedings of the Royal Society A: Mathematical, Physical and Engineering Sciences*, vol. 476, Jan 2020.
- [18] Z. J. Huang, Y. Cao, Y. Y. Sun, Y. Y. Xue, and C. W. Chu, “Coupling between the ferroelectric and antiferromagnetic orders in YMnO<sub>3</sub>,” *Physical Review B*, vol. 56, pp. 2623–2626, Aug 1997.
- [19] Y. Wang, G. L. Pascut, B. Gao, T. A. Tyson, K. Haule, V. Kiryukhin, and S.-W. W. Cheong, “Unveiling hidden ferrimagnetism and giant magnetoelectricity in polar magnet Fe<sub>2</sub>Mo<sub>3</sub>O<sub>8</sub>,” *Scientific Reports*, Jul 2015.
- [20] T. Kurumaji, S. Ishiwata, and Y. Tokura, “Doping-tunable ferrimagnetic phase with large linear magnetoelectric effect in a polar magnet Fe<sub>2</sub>Mo<sub>3</sub>O<sub>8</sub>,” *Physical Review X*, Sep 2015.
- [21] T. Kurumaji, S. Ishiwata, and Y. Tokura, “Diagonal magnetoelectric susceptibility and effect of Fe doping in the polar ferrimagnet Mn<sub>2</sub>Mo<sub>3</sub>O<sub>8</sub>,” *Physical Review B*, vol. 95, pp. 1–9, Jan 2017.
- [22] V. Caignaert, A. Maignan, K. Singh, C. Simon, V. Pralong, B. Raveau, J. F. Mitchell, H. Zheng, A. Huq, and L. C. Chapon, “Gigantic magnetic-field-induced polarization and magnetoelectric coupling in a ferrimagnetic oxide CaBaCo<sub>4</sub>O<sub>7</sub>,” *Physical Review B*, vol. 88, p. 174403, Nov 2013.
- [23] R. D. Johnson, K. Cao, F. Giustino, and P. G. Radaelli, “CaBaCo<sub>4</sub>O<sub>7</sub>: A ferrimagnetic pyroelectric,” *Physical Review B*, Jul 2014.
- [24] K. Singh, V. Caignaert, L. C. Chapon, V. Pralong, B. Raveau, and A. Maignan, “Spin-assisted ferroelectricity in ferrimagnetic CaBaCo<sub>4</sub>O<sub>7</sub>,” *Physical Review B*, vol. 86, p. 024410, Jul 2012.
- [25] Y. S. Oh, S. Artyukhin, J. J. Yang, V. Zapf, J. W. Kim, D. Vanderbilt, and S.-W. Cheong, “Non-hysteretic colossal magnetoelectricity in a collinear antiferromagnet,” *Nature communications*, vol. 5, pp. 1–7, Jan 2014.
- [26] I. Živković, K. Prša, O. Zaharko, and H. Berger, “Ni<sub>3</sub>TeO<sub>6</sub>—a collinear antiferromagnet with ferromagnetic honeycomb planes,” *Journal of Physics Condensed Matter*, vol. 22, Jan 2010.
- [27] L. Zhao, C.-H. Du, and A. C. Komarek, “Spin-driven pyroelectricity in Ni<sub>3</sub>TeO<sub>6</sub> without ferroelectric signatures of the transition at Néel temperature,” *physica status solidi (RRL)*, vol. 11, p. 1700073, Jul 2017.
- [28] S. Ghara, E. Suard, F. Fauth, T. T. Tran, P. S. Halasyamani, A. Iyo, J. Rodríguez-Carvajal, and A. Sundaresan, “Ordered aeschynite-type polar magnets RFeWO<sub>6</sub> (R=Dy, Eu, Tb, and Y): A new family of type-II multiferroics,” *Physical Review B*, vol. 95, p. 224416, Jun 2017.
- [29] P. N. Ravi Shankar, S. Mishra, and S. Athinarayanan, “Polar magnetic oxides from chemical ordering: A new class of multiferroics,” *APL Materials*, vol. 8, Apr 2020.

- [30] S. W. Kim, T. J. Emge, Z. Deng, R. Uppuluri, L. Collins, S. H. Lapidus, C. U. Segre, M. Croft, C. Jin, V. Gopalan, S. V. Kalinin, and M. Greenblatt, “YCrWO<sub>6</sub>: Polar and Magnetic Oxide with CaTa<sub>2</sub>O<sub>6</sub>-Related Structure,” *Chemistry of Materials*, vol. 30, pp. 1045–1054, Feb 2018.
- [31] R. Salmon, H. Baudry, J. Grannec, and G. L. Flem, “Sur de nouvelles séries de composés du tungstène +IV de type aeschynite,” *Revue de Chimie Minérale*, vol. 11, pp. 71–79, 1974.
- [32] K. Yosida, *Theory of magnetism*. Springer series in solid-state sciences, Springer, 1st ed., 1996.
- [33] N. W. Ashcroft and N. D. Mermin, *Solid state physics*. Thomson Learning, Inc., 1976.
- [34] C. Kittel, *Introduction to solid state physics*. Wiley, 8th ed., 2005.
- [35] A. K. Bain and P. Chand, *Ferroelectrics: Principles and applications*. John Wiley & Sons, 2017.
- [36] T. Hahn and H. Klapper, *Crystallographic and noncrystallographic point groups*, vol. A, p. 762–803. International Union of Crystallography, 1st ed., Oct 2006.
- [37] H. Klapper and T. Hahn, *Point-group symmetry and physical properties of crystals*, vol. A, p. 804–808. International Union of Crystallography, 1st ed., Oct 2006.
- [38] A. Devonshire, “Theory of ferroelectrics,” *Advances in Physics*, vol. 3, pp. 85–130, Apr 1954.
- [39] R. W. Whatmore, “Pyroelectric devices and materials,” *Reports on Progress in Physics*, vol. 49, no. 12, pp. 1335–1386, 1986.
- [40] S. B. Lang, “Pyroelectricity: From Ancient Curiosity to Modern Imaging Tool,” *Physics Today*, vol. 58, pp. 31–36, Aug 2005.
- [41] A. P. Levanyuk and D. G. Sannikov, “Improper ferroelectrics,” *Soviet Physics Uspekhi*, vol. 17, pp. 199–214, Feb 1974.
- [42] L. D. Landau and E. M. Lifshitz, *Electrodynamics of continuous media*, vol. 8. Pergamon, 1960.
- [43] I. E. Dzyaloshinskii, “On the magneto-electrical effects in antiferromagnets,” *Soviet Physics JETP*, vol. 10, pp. 628–629, 1960.
- [44] D. Astrov, “Magnetoelectric effect in chromium oxide,” *Soviet Physics JETP*, vol. 13, no. 4, pp. 729–733, 1961.
- [45] S. Dong, H. Xiang, and E. Dagotto, “Magnetoelectricity in multiferroics: a theoretical perspective,” *National Science Review*, vol. 6, pp. 629–641, Feb 2019.
- [46] Y. Tokura, M. Kawasaki, and N. Nagaosa, “Emergent functions of quantum materials,” *Nature Physics*, vol. 13, pp. 1056–1068, Sep 2017.
- [47] H. Schmid, “Multi-ferroic magnetoelectrics,” *Ferroelectrics*, vol. 162, pp. 317–338, Jan 1994.

- [48] J. Wang, J. B. Neaton, H. Zheng, V. Nagarajan, S. B. Ogale, B. Liu, D. Viehland, V. Vaithyanathan, D. G. Schlom, U. V. Waghmare, N. A. Spaldin, K. M. Rabe, M. Wuttig, and R. Ramesh, “Epitaxial BiFeO<sub>3</sub> multiferroic thin film heterostructures,” *science*, vol. 299, pp. 1719–1722, Mar 2003.
- [49] E. Ascher, “Relativistic symmetries and lower bounds for the magneto-electric susceptibility and the ratio of polarization to magnetization in a ferromagneto-electric crystal,” *physica status solidi (b)*, vol. 65, p. 677, 1974.
- [50] R. K. Pathria, *Statistical mechanics*. Butterworth Heinemann, 1996.
- [51] H. Schmid, “On a magnetoelectric classification of materials,” *International Journal of Magnetism J. Magnetism*, vol. 4, pp. 337–361, Jun 1973.
- [52] J.-P. Rivera, “On definitions , units , measurements , tensor forms of the linear magnetoelectric effect and on a new dynamic method applied to Cr-Cl boracite,” *Ferroelectrics*, vol. 161, pp. 165–180, Nov 1994.
- [53] T. Kimura, S. Kawamoto, I. Yamada, M. Azuma, M. Takano, and Y. Tokura, “Magnetocapacitance effect in multiferroic BiMnO<sub>3</sub>,” *Physical Review B*, vol. 67, pp. 2–5, May 2003.
- [54] Y. Tokura, S. Seki, and N. Nagaosa, “Multiferroics of spin origin,” *Reports on Progress in Physics*, vol. 77, p. 076501, Jul 2014.
- [55] M. Fiebig, T. Lottermoser, D. Meier, and M. Trassin, “The evolution of multiferroics,” *Nature Reviews Materials*, vol. 1, p. 16046, Aug 2016.
- [56] I. A. Sergienko and E. Dagotto, “Role of the Dzyaloshinskii-Moriya interaction in multiferroic perovskites,” *Physical Review B*, vol. 73, p. 094434, Mar 2006.
- [57] B. H. Toby and R. B. Von Dreele, “GSAS-II: The genesis of a modern open-source all purpose crystallography software package,” *Journal of Applied Crystallography*, 2013.
- [58] A. Barla, J. Nicolás, D. Cocco, S. M. Valvidares, J. Herrero-Martín, P. Gargiani, J. Moldes, C. Ruget, E. Pellegrin, and S. Ferrer, “Design and performance of BOREAS, the beamline for resonant X-ray absorption and scattering experiments at the ALBA synchrotron light source,” *Journal of Synchrotron Radiation*, vol. 23, pp. 1507–1517, Nov 2016.
- [59] G. Kresse and J. Hafner, “Ab initio molecular-dynamics simulation of the liquid-metal–amorphous-semiconductor transition in germanium,” *Physical Review B*, vol. 49, p. 14251, May 1994.
- [60] G. Kresse and J. Hafner, “Ab initio molecular dynamics for liquid metals,” *Physical Review B*, vol. 47, p. 558, Jan 1993.
- [61] G. Kresse and J. Furthmüller, “Efficiency of ab-initio total energy calculations for metals and semiconductors using a plane-wave basis set,” *Computational materials science*, vol. 6, pp. 15–50, Jul 1996.

- [62] A. H. Larsen, J. J. Mortensen, J. Blomqvist, I. E. Castelli, R. Christensen, M. Dulak, J. Friis, M. N. Groves, B. Hammer, and C. Hargus, “The atomic simulation environment—a Python library for working with atoms,” *Journal of Physics: Condensed Matter*, vol. 29, p. 273002, Jun 2017.
- [63] J. P. Perdew, K. Burke, and M. Ernzerhof, “Generalized gradient approximation made simple,” *Physical review letters*, vol. 77, p. 3865, Oct 1996.
- [64] P. E. Blöchl, “Projector augmented-wave method,” *Physical review B*, vol. 50, p. 17953, Dec 1994.
- [65] G. Kresse and D. Joubert, “From ultrasoft pseudopotentials to the projector augmented-wave method,” *Physical Review B*, vol. 59, no. 3, p. 1758, 1999.
- [66] J. Heyd, G. E. Scuseria, and M. Ernzerhof, “Hybrid functionals based on a screened Coulomb potential,” *The Journal of chemical physics*, vol. 118, pp. 8207–8215, Feb 2003.
- [67] Quantum Design, San Diego, CA, USA, *Physical Property Measurement System Heat Capacity Option User’s Manual*, February 2015.
- [68] C. T. Chen and F. Sette, “High Resolution Soft X-Ray Spectroscopies with the Dragon Beamline,” *Physica Scripta*, vol. T31, pp. 119–126, Jan 1990.
- [69] C. Mitra, Z. Hu, P. Raychaudhuri, S. Wirth, S. I. Csiszar, H. H. Hsieh, H.-J. Lin, C. T. Chen, and L. H. Tjeng, “Direct observation of electron doping in  $\text{La}_{0.7}\text{Ce}_{0.3}\text{MnO}_3$  using X-ray absorption spectroscopy,” *Physical Review B*, vol. 67, p. 092404, Mar 2003.
- [70] T. Burnus, Z. Hu, M. W. Haverkort, J. C. Cezar, D. Flahaut, V. Hardy, A. Maignan, N. B. Brookes, A. Tanaka, H. H. Hsieh, H.-J. Lin, C. T. Chen, and L. H. Tjeng, “Valence, spin, and orbital state of Co ions in one-dimensional  $\text{Ca}_3\text{Co}_2\text{O}_6$ : An X-ray absorption and magnetic circular dichroism study,” *Physical Review B*, vol. 74, p. 245111, Dec 2006.
- [71] T. Burnus, Z. Hu, H. H. Hsieh, V. L. J. Joly, P. A. Joy, M. W. Haverkort, H. Wu, A. Tanaka, H.-J. Lin, C. T. Chen, and L. H. Tjeng, “Local electronic structure and magnetic properties of  $\text{LaMn}_{0.5}\text{Co}_{0.5}\text{O}_3$  studied by X-ray absorption and magnetic circular dichroism spectroscopy,” *Physical Review B*, vol. 77, p. 125124, Mar 2008.
- [72] B. T. Thole, P. Carra, F. Sette, and G. van der Laan, “X-ray circular dichroism as a probe of orbital magnetization,” *Physical Review Letters*, vol. 68, pp. 1943–1946, Mar 1992.
- [73] P. Carra, B. T. Thole, M. Altarelli, and X. Wang, “X-ray circular dichroism and local magnetic fields,” *Physical Review Letters*, vol. 70, pp. 694–697, Feb 1993.
- [74] M. Adnani, M. Gooch, L. Deng, S. Agrestini, J. Herrero-Martin, H.-C. Wu, C.-k. Chang, T. Salavati-fard, N. Poudel, J. L. García-Muñoz, S. Daneshmandi, Z. Wu, L. C. Grabow, Y.-C. Lai, H.-D. Yang, E. Pellegrin, and C. W. Chu, “Magnetocapacitance effect and magnetoelectric coupling in type-II multiferroic  $\text{HoFeWO}_6$ ,” *Physical Review B*, vol. 103, p. 094110, Mar 2021.
- [75] A. Tanaka and T. Jo, “Resonant 3d , 3p and 3s Photoemission in Transition Metal Oxides Predicted at 2p Threshold,” *Journal of the Physical Society of Japan*, vol. 63, pp. 2788–2807, Jul 1994.

- [76] A. N. Vasiliev, O. S. Volkova, E. A. Zvereva, and M. Markina, *Low-Dimensional Magnetism*. CRC Press, 2019.
- [77] A. A. Bokov and Z.-G. Ye, “Dielectric relaxation in relaxor ferroelectrics,” *Journal of Advanced Dielectrics*, vol. 02, p. 1241010, Apr 2012.